Check for updates

Cite as: H. Zhou *et al.*, *Science* 10.1126/science.aei5957 (2026).

In situ structure of the human ciliary transition zone links linker defects to primary ciliary dyskinesia

Haixia Zhou[1]†, Lea Terbeck[2]†, Andrew Berical[3,4], Marine Brunet[5], Sven M. Lange[1], Jacob R. Anderson[1], Heike Olbrich[2], Diana Carolin Bracht[2], Kai Wohlgemuth[2], Cynthia Rieck[2], Johanna Raidt[2], Jürgen Klingauf[6], Sivagurunathan Sutharsan[7], Huda Mussaffi[8], Dario Prais[8], Victoria Dunphy[3,4], Sachiko T. Homma[3,4], Paul Guichard[5], Virginie Hamel[5], Finn J. Hawkins[3,4], Heymut Omran[2]*, Alan Brown[1]*

[1]Department of Biological Chemistry and Molecular Pharmacology, Blavatnik Institute, Harvard Medical School, Boston, MA, USA. [2]Department of General Pediatrics, University Children's Hospital Münster, Münster, Germany. [3]Center for Regenerative Medicine of Boston University and Boston Medical Center, Boston, MA, USA. [4]The Pulmonary Center, Boston University Chobanian & Avedisian School of Medicine, Boston, MA, USA. [5]Department of Molecular and Cellular Biology, Sciences III, University of Geneva, Geneva, Switzerland. [6]Institute of Medical Physics and Biophysics, University of Münster, Münster, Germany. [7]Department of Pulmonary Medicine, University Hospital Essen - Ruhrlandklinik, University of Duisburg-Essen, Essen, Germany. [8]Pulmonary Institute, Schneider Children's Medical Center, Petah Tikva, Israel, Gray Faculty of Medical and Health Sciences, Tel Aviv University, Tel Aviv, Israel.

†These authors contributed equally to this work

***Corresponding author. Email:** Heymut.Omran@ukmuenster.de (H.O.); alan_brown@hms.harvard.edu (A.B.)

The ciliary transition zone (TZ) regulates ciliary proteome composition, yet its molecular architecture, protein content, and contribution to motile ciliopathies remain poorly defined. We applied in situ cryo-electron tomography and subtomogram averaging to human multiciliated epithelial cells. This approach resolved TZ-specific doublet microtubules at subnanometer resolution and identified nine constituent proteins. We identified that ECT2L and DZANK1 form the major linker complexes between adjacent TZ doublet microtubules. Biallelic loss-of-function variants in either gene cause primary ciliary dyskinesia. *ECT2L* and *DZANK1* deficiency disrupted TZ architecture, caused microtubular abnormalities and abnormal bulbous ciliary tips, and impaired mucociliary clearance. These findings establish a direct genetic link between TZ defects and human motile ciliopathy, and illustrate how in situ structural biology can uncover mechanisms of human disease.

Cilia are microtubule-based organelles that project from the surface of most eukaryotic cells, where they generate motility or transduce signals. Ciliary proteomes are shaped by the transition zone (TZ), a specialized region at the ciliary base that functions as a molecular gate, selectively excluding some proteins while retaining or concentrating others (*1*). Ciliary entry is often licensed by dedicated targeting sequences (*2*), whereas protein removal is frequently triggered by polyubiquitination (*3–5*). Despite these insights, the molecular mechanisms by which cargos and motors physically traverse the TZ remain poorly defined.

In mammalian cilia, the TZ also coincides with the structural transition from basal-body triplet microtubules (TMTs) to axonemal doublet microtubules (DMTs). Ex situ cryo-electron tomography (cryo-ET) of basal-body-axoneme complexes from bovine respiratory cilia revealed that DMTs within the TZ are structurally distinct from axonemal DMTs (*6*). Two defining features are shelf-like microtubule inner proteins (MIPs) decorating both the A- and B-tubules, and linker complexes connecting the A tubule of one DMT to the B tubule of its neighboring DMT. These "TZ linkers" are thought to provide lateral connectivity and structural integrity, but their protein composition is unknown, which complicates understanding their function.

Disease-causing variants in genes encoding TZ proteins underlie ciliopathies associated with dysfunction of primary (non-motile) cilia, including Joubert syndrome, Meckel–Gruber syndrome, nephronophthisis, Senior-Løken syndrome, and Leber congenital amaurosis (*7*). In contrast, the genetic basis of motile ciliopathies, such as primary ciliary dyskinesia (PCD), usually involves loss-of-function variants in axoneme-related genes (*8*). The lack of variants in TZ-related genes in inherited motile ciliopathies has implicitly suggested that the gating functions of the TZ may be dispensable for motile cilia function.

In situ cryo-ET of the human motile ciliary transition zone

To elucidate the molecular composition of TZ microtubules and their linkers in human motile cilia, we performed in situ cryo-ET of human respiratory cilia (Fig. 1A and table S1). Primary human nasal epithelial cells were cultured and differentiated at the air-liquid interface (ALI) until robust ciliogenesis was observed. Fully differentiated cell cultures were dissociated into single cells or small multicellular clusters using mechanical force and plunge-frozen onto cryo-EM grids. Focused ion beam (FIB) milling was performed on the periphery of the frozen ciliated cells, generating thin lamellae suitable for cryo-ET (fig. S1). The resulting tomograms revealed ciliary bases enveloped by deep plasma membrane

Downloaded from https://www.science.org at Cornell University on September 14, 2026

invaginations known as ciliary pockets (Fig. 1, B, C, and E). Prominent densities corresponding to the ciliary necklace, a hallmark of the TZ membrane subdomain (*9*), were observed within the pocket membrane adjacent to the ciliary microtubules. Y-link densities connecting the ciliary necklace to the underlying DMTs were also present but, as expected from tomography of mouse ependymal cilia (*10*), were less pronounced than the Y links in *C. reinhardtii* (*11*).

The TZ is distinguished by a narrowing of the microtubule ring diameter relative to basal-body and axonemal DMTs (Fig. 1, B and D). Periodic striations within the TZ DMTs (Fig. 1, B and E) indicated shelf-like MIPs, as seen with bovine respiratory cilia (*6*). These striations enabled targeted subtomogram averaging, and the resulting averages revealed well-defined DMTs with 8-nm longitudinal periodicity. Attempts to resolve higher-order periodicity through three-dimensional classification were unsuccessful, indicating that 8 nm is the dominant repeat. Local resolution was further improved through individual protofilament refinements and classifications that were subsequently combined into a composite map at 6.9–7.3 Å resolution (figs. S1 and S2). This map was used to reconstruct the ring-like assembly of nine TZ DMTs (Fig. 2A).

Identification of TZ microtubule inner proteins

Subtomogram averaging and prior work enabled the identification of four MIPs within human TZ DMTs (Fig. 2B): CFAP20, CEP41, ENKD1, and calcyphosine-family proteins. CFAP20 localizes to the inner junction where it connects the A and B tubules (Fig. 2C), as it does along axonemal DMTs in every cilium type studied to date (*12*, *13*). CEP41 binds protofilaments B01–B02 near the outer junction (Fig. 2D), where its AlphaFold2-predicted atomic model provided the best fit to the density among all human protein domains tested (fig. S3A). Although CEP41 binds TZ DMTs, it is unlikely to be TZ-specific, because it also localizes to basal-body TMTs and proximal axonemal DMTs of mouse ependymal cilia (*10*) (fig. S3B). Density that penetrates the interface between protofilaments B09–B10 likely corresponds to ENKD1 (Fig. 2E and fig. S3) because an analogous position is occupied by its paralog ENKUR in axonemal DMTs (*12*, *13*). We used ultrastructural expansion microscopy (U-ExM) to assess these paralog distributions: ENKD1 was restricted to the proximal cilium, including the TZ and basal body, whereas ENKUR localized along the axoneme (fig. S3, F and G).

We assigned the prominent shelf-like densities within TZ DMTs to calcyphosine-family proteins (Fig. 2, F and G) based on fold recognition (see the Materials and methods and fig. S4, A and B). In humans, this microtubule-binding family (*14*) comprises three paralogs – CAPS, CAPSL, and CAPS2 (fig. S4C) – each with two globular domains containing paired calcium-binding EF-hand motifs (*15*). CAPS/CAPSL homologs are broadly conserved across ciliated organisms (fig. S5A and data S1) and are transcriptionally induced by the motile ciliogenesis factor FOXJ1 (*16*). Single-cell RNA sequencing (scRNA-seq) showed that all three paralogs were expressed in multiciliated lung epithelial cells (fig. S4D). U-ExM confirmed CAPSL and CAPS2 at the TZ of multiciliated respiratory epithelial cells (fig. S4, E to G), whereas the CAPS antibody gave largely nonspecific signal. CAPSL is likely the predominant calcyphosine species at the TZ and could be distinguished from its paralogs by an N-terminal CAPSL-specific helix (Fig. 2G). Consistent with its strong U-ExM signal, CAPSL was present in multiple copies per 8-nm repeat (Fig. 2H), with some copies showing substoichiometric binding or potentially mixed occupancy with its paralogs (Fig. 2H, asterisks).

The CAPSL arrangement on TZ DMTs resembled that of another shelf-like MIP, SPACA9, which forms striations in human sperm singlet microtubules and axonemal B tubules (fig. S4H) (*12*). Both proteins favor multi-protofilament interfaces and display substoichiometric or variable occupancy at specific protofilaments. However, their binding sites differ: SPACA9 primarily contacts the α/β-tubulin interface (*12*), whereas CAPSL mainly recognizes α-tubulin, with only minor contributions from β-tubulin (Fig. 2G) and the lateral α-tubulin neighbor. In summary, our data showed that human TZ DMTs are internally decorated by CFAP20, CEP41, ENKD1, and the calcyphosine family.

MAP9 binds the B-tubule exterior

The external surfaces of TZ DMTs are decorated by several microtubule-associated proteins (fig. S6A). Among them, we identified a single curved α-helix, measuring ~300 Å in length, stretching laterally across five B-tubule protofilaments (B02–B06) (Fig. 2, B and I). Several converging lines of evidence support assignment of this helix to microtubule-associated protein 9 (MAP9). First, its length, curved geometry, and lateral binding across protofilaments precisely match a recent cryo-EM structure of MAP9 bound to in vitro assembled singlet microtubules (*17*). This structure shows that the microtubule-binding α-helix of MAP9 (residues 420–623) contains five conserved and equally spaced microtubule-binding motifs that interact directly with β-tubulin on neighboring protofilaments. An AlphaFold2-predicted model of the MAP9 microtubule-binding helix fitted our density well and positioned each motif near the expected β-tubulin-binding site (Fig. 2I). Second, scRNA-seq confirmed *MAP9* expression in multiciliated epithelial cells (fig. S6B) and U-ExM detected MAP9 at the TZ of human respiratory cilia (fig. S6C). This localization agrees with prior fluorescence microscopy identifying MAP9 and its orthologs at the proximal cilium across diverse species and cell types, including the cilia of *C. elegans* and mammalian kidney collecting duct cells, nasal

Downloaded from https://www.science.org at Cornell University on September 14, 2026

epithelium, photoreceptors, and sperm flagella (*18*–*20*). Third, our assignment is consistent with genetic disruption of the *C. elegans* MAP9 ortholog MAPH-9, which causes axonemal DMT loss and abnormal B-tubule architecture in the remaining DMTs (*18*). These defects point to a specific role for MAP9 in B-tubule stabilization, consistent with the location and characteristics of the density observed here. Although we identified MAP9 as a B-tubule-binding protein at the TZ of motile cilia, it also associates with other microtubule populations, decorating interphase and mitotic microtubules in human U-2 OS cells (*21*) and localizing throughout dendrites and axons in primary mouse hippocampal neurons (*22*).

ECT2L is a core component of TZ linkers

Adjacent TZ DMTs are connected by linkers (Fig. 2A) that bridge protofilament B07 of one DMT to protofilaments A06–A07 of the neighbor (*6*). To resolve the architecture and molecular composition of these linkers, we performed focused refinement and classification specifically of TZ linker density (fig. S1). Classification was necessary because both U-ExM and subtomogram averaging showed that TZ linkers do not extend as far into the cilium as CAPSL (fig. S7 and data S2), indicating that different zones exist even within the TZ. This targeted classification approach yielded an ~8-Å resolution reconstruction with sufficient detail to resolve multiple globular domains (Fig. 3A).

To identify protein constituents, we performed automated segmentation of the TZ linker density, followed by an unbiased screen to systematically fit a library of 28,142 AlphaFold2-predicted domains from 16,396 human proteins independently to each segmented density (*23*) (Fig. 3B). Each fit was scored using a local z-score metric (see the Materials and methods). The screen repeatedly identified domains from epithelial cell transforming 2 like (ECT2L) as the top-scoring matches for five of six distinct segmented densities (fig. S8A). The presence of the same domain in neighboring segmented densities suggested that ECT2L forms a homodimer within the TZ linker. ECT2L is a paralog of the oncogenic ECT2 protein (*24*). However, the two proteins share only their C-terminal architecture, with both ending in tandem Dbl homology (DH) and pleckstrin homology (PH) domains (Fig. 3C and fig. S9A). The N-terminal region of ECT2L contains a dimerization (D) domain, an F-box, and a domain of unknown function (DUF), whereas ECT2 possesses three N-terminal BRCT domains. Detection of the ECT2L DUF domain but not ECT2 BRCT domains excluded ECT2 as a candidate. This DUF domain occurs in only one other human protein, NSMF (fig. S9, A and B), which lacks additional domains and was also excluded.

ECT2L homologs are present in many, but not all, metazoan lineages (fig. S5A and data S1), suggesting a complex evolutionary history or multiple independent losses. In humans, *ECT2L* expression is highest in ciliated tissues (*25*). Single-cell RNA sequencing detected *ECT2L* predominantly in the multiciliated epithelial cells of the lung (*26*) (fig. S9C) and of the fallopian tube (fig. S10A). In zebrafish, *ect2l* transcripts are up-regulated upon Foxj1 overexpression, and morpholino-mediated *ect2l* knockdown produces short cilia and a curved body axis – phenotypes characteristic of ciliary dysfunction (*16*). Super-resolution immunofluorescence microscopy further confirmed ECT2L localization to the ciliary base in motile cilia of multiciliated airway cells (Fig. 3D), where it colocalized with TZ marker NPHP1 and localized above the basal-foot marker CNTRL (fig. S9E). Immunofluorescence analysis of healthy human fallopian tube epithelium showed the same ciliary base localization (fig. S10B). These orthogonal data establish ECT2L as a ciliary protein that localizes to the TZ of motile cilia.

ECT2L N-terminal domains bind microtubules and SKP1

Guided by density and structural predictions, we placed all five domains of ECT2L within the linker reconstruction. The structure reveals an asymmetric homodimer (Fig. 3, E and F) with extensive interdomain interactions, particularly among the DUF, DH and PH domains. The N-terminal D domain and F-box of each monomer are connected to the DUF domain through a flexible, nonconserved linker that is not resolved in the subtomogram average.

Our structure shows that the N-terminal dimerization (D) domain serves dual roles: it mediates ECT2L homodimerization by intertwining three helices from each monomer (Fig. 3F) and directly interacts with the microtubule surface on protofilament B07 (Fig. 3E). Density adjacent to both F-boxes was independently identified as SKP1 using domain recognition (fig. S8B), consistent with SKP1 being a canonical F-box partner. Although SKP1 is ubiquitous and abundant in most cell types (fig. S9D), U-ExM and super-resolution microscopy revealed specific SKP1 signal at the TZ (Fig. 3G and fig. S9F). We therefore conclude that a major component of the TZ linker is an ECT2L–SKP1 heterotetramer with 2:2 stoichiometry.

ECT2L modules are occluded in the TZ linker

The pairing of an N-terminal D domain with an F-box motif is characteristic of several Skp1–Cullin–F-box (SCF) E3 ubiquitin ligase adaptors. Although AlphaFold3 confidently predicted an ECT2L–SKP1–CUL1–RBX1 complex (fig. S11, A and B), the CUL1-binding surfaces of both F-box motifs are occluded in the tetrameric ECT2L–SKP1 arrangement (fig. S11C). ECT2L may therefore be another F-box protein that binds SKP1 without forming an active ligase (*27*, *28*).

The C-terminal DH–PH module of ECT2L resembles those of

Downloaded from https://www.science.org at Cornell University on September 14, 2026

Dbl family RhoGEFs (*29*) and is 29% identical to the ECT2 DH–PH module, which has experimentally validated RhoGEF activity (*24*, *30*). However, AlphaFold2-Multimer predicted no interactions between the ECT2L DH–PH module and human Rho GTPases, although the same screen recovered the known ECT2–GTPase pairs (fig. S11D and data S5). A kink in the ECT2L DH α6 helix could sterically block GTPase binding (fig. S11E). Moreover, even if ECT2L has retained RhoGEF activity, the putative GTPase-binding site is buried in the TZ linker conformation (fig. S11F).

ECT2L therefore carries modules associated with both RhoGEF and E3 ligase activity, yet the linker conformation buries the binding surfaces that each activity requires.

DZANK1 partners ECT2L in TZ linkers

Structural modeling of the ECT2L–SKP1 complex revealed additional density between adjacent ECT2L homodimers (Fig. 3E, pink asterisks), suggesting another component. To identify this factor, we performed an all-against-ECT2L interaction screen using AlphaFold2-Multimer (*31*) and a curated set of 2,729 human ciliary proteins (*5*). The two highest-scoring interactions were with itself and SKP1 (Fig. 4A), consistent with ECT2L homodimerization and SKP1 recruitment via its F-box motif. The fourth highest-scoring candidate was double zinc ribbon and ankyrin repeat-containing protein 1 (DZANK1) (Fig. 4, A to C), an interaction we validated by co-precipitation experiments (Fig. 4D). A reciprocal search starting with DZANK1 also identified ECT2L as its top-scoring partner (fig. S12A). Supporting a ciliary function, DZANK1 is transcriptionally regulated by the ciliogenesis master regulator FOXJ1 (*16*). It was enriched in multiciliated epithelial respiratory cells (fig. S12B) and localized to the TZ by U-ExM (Fig. 4E and fig. S12C) and super-resolution immunofluorescence (fig. S12D). *DZANK1* is also expressed in multiciliated epithelial cells of the human fallopian tube (fig. S10B) and in mouse ependymal cells (fig. S10C), and, unlike *ECT2L*, in photoreceptors (fig. S10D).

DZANK1 is a multidomain protein with an N-terminal immunoglobulin-like domain, five zinc-binding domains, and a C-terminal ankyrin repeat region (Fig. 4C). The zinc-binding domains are predicted to bind the ECT2L F-box (Fig. 4, B and F). Although these small domains could not be modeled unambiguously in the relatively weak density, the subtomogram map was consistent with their presence (Fig. 3E). DZANK1 thus bridges ECT2L–SKP1 heterotetramers in the TZ linker through its zinc-binding domains.

DZANK1 and DYNLL1/2 tether TZ linkers to the A tubule

We next asked how TZ linkers attach to the neighboring A tubule. Subtomogram averaging revealed two globular densities on protofilaments A06 and A07, connected by a single helix (Fig. 3E, blue and purple asterisks). Although these densities did not match known globular DZANK1 domains, AlphaFold3 predicted a previously unannotated dimerization domain in DZANK1 (residues 466–535; fig. S12E), which fitted the A06 density (Fig. 4G and fig. S12F). Immediately upstream, an α-helix (residues 443–465) likely corresponds to the bridging helix that extends to protofilament A07. Upstream further, a conserved TQT motif (residues 433–435; Fig. 4, C and G) forms a canonical DYNLL1/2-binding site, consistent with the reported DZANK1–DYNLL1 interaction (*32*). AlphaFold3 modeling of DZANK1 bound to a DYNLL1 homodimer supported this assignment (fig. S12G) and fully accounted for the A07 density (Fig. 4G and fig. S12H). DYNLL2 is an equally plausible partner, given its 93% identity to DYNLL1, expression in lung multiciliated epithelial cells (fig. S5B), and distribution along the cilium (fig. S12I).

These observations together indicate that TZ linkers are linear arrays of ECT2L–SKP1–DZANK1–DYNLL1/2 complexes (Fig. 4H). The positions of N-terminal immunoglobulin-like and C-terminal ankyrin repeat domains of DZANK1 remain uncertain but may correspond to weak inward-projecting density from the TZ linker (Fig. 3E, green asterisk).

ECT2L and DZANK1 variants cause primary ciliary dyskinesia

We hypothesized that loss-of-function variants in TZ linker components could cause primary ciliary dyskinesia (PCD). To test this hypothesis, we analyzed a cohort of 489 individuals with suspected PCD for variants in all identified TZ-linker proteins and identified four unrelated individuals with predicted loss-of-function variants: three with distinct biallelic *ECT2L* variants (Fig. 5, A and B, and fig. S13) and one with a *DZANK1* variant (Fig. 5, C and D).

For *ECT2L*, individual OP-2226 II1 carries two pathogenic variants: a single-nucleotide duplication (c.155dup, p.(Leu52PhefsTer5)) and a nonsense variant (c.2227C>T, (p.Gln743Ter)), both of which are predicted to terminate translation prematurely. Individual OI-70 II1 carries the same nonsense variant plus a splice-site deletion (c.2028+1_2028+18delinsTTTA, p.Arg627LysfsTer5). Individual OP-198 II1 is homozygous for this splice-site deletion (c.2028+1_2028+18delinsTTTA, p.Arg627LysfsTer5). cDNA analysis showed that exon 16 was skipped, causing a frameshift and introducing a premature termination codon (fig. S13D). Consistent with these predicted loss-of-function effects, we observed nonsense-mediated mRNA decay from both OP-2226 II1 and OP-198 II1 (fig. S14A). Immunofluorescence analysis of patient-derived multiciliated nasal cells (OI-70 II1) and ALI-cultured multiciliated respiratory cells (OP-2226 II1, OP-198 II1) confirmed loss of ECT2L and SKP1 from the TZ in all three individuals, whereas DZANK1 localization remained intact (Fig. 5E and figs. S15 to S17).

Downloaded from https://www.science.org at Cornell University on September 14, 2026

Individual OP-3278 II1 is an offspring of consanguineous parents and carries a homozygous *DZANK1* frameshift variant (c.1758dup, p.(Leu587AlafsTer11)) that is predicted to cause premature translation termination (Fig. 5D and fig. S13E). Parental DNA for segregation analyses was unavailable. The gnomAD v4.1 frequency for this variant is very low (0.00000958), and only heterozygous variants were observed. Consistent with the prediction of premature termination of translation, cDNA analyses showed evidence of nonsense-mediated mRNA decay (fig. S14B). Complete loss of the DZANK1 protein was confirmed by immunoblotting (fig. S14C) and immunofluorescence analyses (Fig. 5E and fig. S17). At the TZ, ECT2L and SKP1 were also undetectable or severely reduced (Fig. 5E and figs. S15 to S16), indicating that DZANK1 is required for proper ECT2L assembly within the TZ linker.

All four individuals presented with hallmark clinical features of PCD, including chronic wet cough, recurrent rhinosinusitis, chronic atelectasis, and bronchiectasis (Fig. 5, F and G, and table S2). Nasal nitric oxide production rates, a quantitative biomarker frequently reduced in PCD individuals, were below the diagnostic threshold (77 nl/min) (*33*) for all four cases in all but one measurement (table S2).

ECT2L and DZANK1 loss disrupts TZ architecture and ciliary function

Transmission electron microscopy (TEM) of ALI-differentiated multiciliated respiratory epithelium of healthy controls showed canonical TZ architecture, with nine DMTs and intact TZ linkers in nearly all sections examined (Fig. 6, A and B, and fig. S18). In contrast, samples from *ECT2L*-variant individuals OP-2226 II1 and OP-198 II1 and *DZANK1*-variant individual OP-3278 II1 displayed severely disrupted TZs, with frequent abnormal cross sections (Fig. 6, A and B, and fig. S18; OP-198 II1: 11% with abnormalities, OP-2226 II1: 61%, OP-3278 II1: 42%). DMTs were irregularly spaced and often lacked discernible TZ linkers (OP-198 II1: 30% without linkers, OP-2226 II1: 83%, OP-3278 II1: 100%). Complete loss of TZ linkers in OP-3278 II1 cells is consistent with immunofluorescence analysis, which demonstrated the absence of ECT2L, DZANK1 and SKP1 from the TZ (figs. S15 to S17). Together, these results establish ECT2L and DZANK1 as essential components for proper TZ DMT organization and structural integrity.

Disrupted TZ organization also appears to impact the axoneme, with >40% of axonemal cross sections from OP-2226 II1 and OP-3278 II1 showing microtubule defects (Fig. 6C and fig. S19). Scanning electron microscopy (SEM) further revealed occasional elongated cilia and cilia ending in atypical bulbous tips in *ECT2L*- and *DZANK1*-deficient cultures (Fig. 6D and fig. S20A). High-speed video microscopy (HSVM) analyses of trypsinized cells from ALI cultures (movie S1) confirmed frequent bulbous tips (Fig. 6E; OP-198 II1: 75% of movies, OP-2226 II1: 19%, and OP-3278 II1: 89%). The bulbous tips often contained electron-dense cytoplasmic inclusions or collapsed axonemal structures (fig. S20B). Similar tip swellings occur in human disorders affecting retrograde intraflagellar transport (IFT), including variants in dynein-2 motor subunits (*34–37*), IFT-A subunits (*38*, *39*), and IFT regulators (*40*). Using immunofluorescence analysis, we demonstrated the accumulation of IFT88 in the bulbous tips of cells from OP-198 II1 and OP-3278 II1 (fig. S20C), supporting the idea that they represent a buildup of IFT proteins and associated cargos not efficiently cleared by retrograde transport. This interpretation is consistent with the known role of the TZ as a selective barrier regulating IFT flux and indicates that variants in TZ-associated genes can impair transport proteostasis in motile cilia.

HSVM analysis revealed that ciliary beat frequencies (CBFs) in *ECT2L*- and *DZANK1*-variant cells were within the lower normal range (Fig. 6F) but beat patterns were heterogeneous, with regions of normal ciliary beating interspersed with cilia showing reduced amplitude and uncoordinated beating (movie S1). Consistent with more severe disruption of the TZ linkers, the *DZANK1*-variant individual showed severely uncoordinated beating.

To assess functional consequences of the disrupted TZ linkers, we performed ciliary transport assays (*41*) on ALI cultures (Fig. 6G and movie S2). Compared to healthy controls, mean transport velocities of fluorescent particles were significantly reduced in *ECT2L*-deficient cultures and showed no active transport in *DZANK1*-deficient cultures. This indicates impaired mucociliary clearance despite near-normal CBFs. These structural and functional defects are consistent with the clinical presentation of PCD in *ECT2L*- and *DZANK1*-variant individuals. Thus, we identified pathogenic variants in two distinct genes responsible for the disruption of the previously uncharacterized TZ linker.

CRISPR-Cas9-mediated ECT2L knockout recapitulates disease-associated phenotypes

To confirm that ciliary defects in patient samples result from *ECT2L* loss rather than unknown modifiers, we used CRISPR-Cas9 gene editing to specifically ablate *ECT2L* from healthy donor basal cells in an established induced pluripotent stem cell (iPSC)-directed differentiation system (*42*, *43*) (fig. S21, A and B). Following basal cell differentiation into a mucociliary epithelium, RT-qPCR analysis confirmed substantial reduction of *ECT2L* expression in knockout (KO) compared to non-targeted guide control (NTC) cultures, consistent with nonsense-mediated decay, while markers for ciliogenesis (*FOXJ1*) and motile cilia (*DNAH5* and *CCDC40)* remained unchanged between NTC and *ECT2L-KO* cultures, ruling out global perturbation of ciliary gene expression (fig. S21C). Immunoblot analysis confirmed loss of ECT2L protein within

Downloaded from https://www.science.org at Cornell University on September 14, 2026

ECT2L-KO differentiated mucociliary epithelial cultures compared to NTC cultures (fig. S21D) and immunofluorescence analysis confirmed specific loss of ECT2L from the TZ (fig. S21E). Electron microscopy of *ECT2L*-KO cultures revealed widespread bulbous ciliary tips (fig. S21, F and G) that directly recapitulated the morphology observed in multiciliated cells derived from affected individuals. These findings provide functional validation that *ECT2L* loss of function underlies the ciliary defects associated with genetic PCD.

Discussion

Here, by combining in situ cryo-ET with human genetics, we generated an atomic model of transition zone doublet microtubules (TZ DMTs) in human multiciliated epithelial cells and identified variants in proteins linking neighboring TZ DMTs (ECT2L and DZANK1) as previously unrecognized causes of primary ciliary dyskinesia (PCD).

MAP9 is positioned to regulate intraflagellar transport

Our finding that MAP9 decorates B-tubule protofilaments likely used by kinesin-2 (*44*) provides a foundation for understanding how the TZ regulates IFT. Recent work shows that MAP9 engages kinesin motors through a divergent loop (loop 8) in their microtubule-binding domains, thereby conferring motor selectivity (*17*). If analogous interactions occur between MAP9 and kinesin-2 in vivo, they could explain why the *C. elegans* MAP9 ortholog differentially regulates three IFT motors: slowing heterotrimeric kinesin-II and dynein while promoting homodimeric OSM-3 function (*18*). Together, these data support a model in which MAP9 functions as a selective gatekeeper, permitting specific motors to engage the B-tubule track while restricting others. Such selective engagement could regulate the entry of anterograde IFT trains into cilia or enforce their segregation to the B tubule. MAP9 may thus constitute a functional equivalent to the sleeve structure that decorates the exterior of distal TZ DMTs in *C. reinhardtii* flagella and has been proposed to act as a spatial barrier to regulate IFT entry or exit by hindering attachment of molecular motors to the microtubule (*11*).

Structural diversity of TZ linkers across human cilium types

Expression data indicate that the TZ linker composition defined here is likely conserved across other mammalian motile cilia, given the expression of both *DZANK1* and *ECT2L* in human fallopian tube multiciliated cells and in mouse brain ependymal cells. However, primary cilia appear to rely on fundamentally different microtubule-tethering mechanisms. For example, the photoreceptor connecting cilium, the structural and functional equivalent of the motile cilium TZ, features an inner scaffold complex that is compositionally and architecturally distinct from the TZ linkers described here (*45*). This structural divergence is reflected in cell-specific expression profiles: although DZANK1 is present in photoreceptors and localizes to the connecting cilium in mature retina (*32*), ECT2L is undetectable. These observations, together with the presence of DZANK1 homologs in species that lack ECT2L, raise the possibility that DZANK1 might perform cilium-type-specific functions independent of ECT2L (*32*).

Motile cilia TZ disruption causes PCD

Our identification of loss-of-function variants in *ECT2L* and *DZANK1* in individuals with PCD establishes a direct link between TZ defects and motile ciliopathies, whereas TZ dysfunction had historically been associated exclusively with nonmotile ciliopathies. Our findings extend the spectrum of TZ-linked disease to motile cilia and indicate that disruption of TZ architecture can impair mucociliary clearance. Additional evidence suggests that other perturbations in the TZ beyond defects in the TZ linker can cause motile ciliary dysfunction. For example, mice lacking KIF27, a protein reported to reside at the TZ but not observed in our structural analyses, display phenotypes characteristic of PCD (*46*).

In *ECT2L*- and *DZANK1*-variant cultures, we observed marked disruption of TZ architecture, including loss of the canonical ring-like arrangement of nine TZ DMTs, with the defects propagating into the axoneme as frequent departures from the 9+2 organization. These structural abnormalities coincided with the presence of bulbous ciliary tips that contained cytoplasmic inclusions, collapsed axonemal structures, and IFT88, features reminiscent of impaired retrograde IFT. We propose that the breakdown of the TZ barrier perturbs ciliary proteostasis, either allowing nonciliary proteins to accumulate within the cilium or by disrupting proper IFT movement. The resulting bulbous tips likely alter ciliary packing and beat geometry, compromising the coordinated, high-amplitude effective strokes necessary for efficient fluid flow and thus efficient mucociliary clearance in *ECT2L*- and *DZANK1*-variant individuals. Together, our findings combine in situ structural biology with human genetics to define the molecular architecture of TZ DMTs in human motile cilia and to establish TZ-linker defects as a direct cause of PCD.

Materials and methods

Human studies

This research was approved by the Ethics Committee of the Medical Association of Westphalia-Lippe and the University of Münster (study code: 2015-104-f-S). Signed informed consent was obtained from participants, legal guardians, and/or relatives according to protocols approved by the Institutional Ethics Review Board of the University of Münster and collaborating institutions.

Downloaded from https://www.science.org at Cornell University on September 14, 2026

Air-liquid interface (ALI) cultures

Human nasal cells were collected by brushing the inferior nasal turbinate of a healthy donor with a sterile nasal curette (Arlington Scientific, #0425). Cells were mechanically dislodged from the brush and seeded onto collagen-coated (PureCol, Sigma-Aldrich, #5006-15MG) 12-well plates (Corning, #3513) in PneumaCult-Ex Plus media (STEMCELL Technologies, #05040). Cells were passaged twice, first into a T25 flask and then onto 12 Transwell inserts (Corning, #CLS3460) at a density of ~0.5-1.0 $\times 10^6$ cells per insert. After reaching confluence in PneumaCult-Ex Plus medium, the basolateral medium was replaced with PneumaCult-ALI medium (STEMCELL Technologies, #05001), and the apical surface was exposed to air. All media contained Primocin (InvivoGen, #ant-pm-05) and Penicillin-Streptomycin (Thermo Fisher Scientific, #15070063). Ciliation was observed 3–4 weeks after transition to ALI. During differentiation, basolateral medium was refreshed every 2 days, and apical surfaces were washed weekly with Dulbecco's phosphate-buffered saline (DPBS) to remove mucus.

Cryo-ET grid preparation

Cells were dissociated from Transwells by incubation with Accutase (STEMCELL Technologies, #07920) for 15 min at 37°C to generate single-cell suspensions with minimal clumping. Cells were washed twice with DPBS and then suspended in PneumaCult-ALI medium at 1 $\times 10^7$ cells/mL. Aliquots (3 μL) of cell suspension were applied to glow-discharged QUANTIFOIL R3.5/1, 300-mesh gold grids (Electron Microscopy Sciences, #Q350AR-35) mounted in a Vitrobot Mark IV (Thermo Fisher Scientific). Grids were blotted from the back for 8 s with a blot force of 10 and 100% humidity before being plunged into liquid ethane cooled by liquid nitrogen. For back-blotting, filter paper on the sample side was replaced with Parafilm.

Cryo-focused ion beam (FIB) milling

Lamella preparation was performed on an Aquilos 2 cryo-FIB/SEM (Thermo Fisher Scientific). To screen grids and adjust focus, a scanning electron microscopy (SEM) map of the entire grid was acquired at 64× magnification using an acceleration voltage of 5 kV with a beam current of 13 pA and a dwell time of 1 μs. Higher-resolution maps of selected grids were acquired at 2 kV voltage using Maps v.3.21 (Thermo Fisher Scientific). Cells or small clusters of cells with appropriate thickness for milling were selected on the map. A platinum layer was sputter-coated at 30 mA and 10 Pa for 15 s, followed by gas injection system (GIS) deposition of trimethyl(methylcyclopentadienyl)platinum (IV) precursor for 45–60 s depending on target thickness, and then by another round of sputter coating using identical settings. Milling angles were automatically defined by AutoTEM Cryo v2.4 (Thermo Fisher Scientific). FIB milling was performed in AutoTEM Cryo using stepwise decreasing currents as the lamellae were thinned (1.0 nA–30 pA; final thickness, ~200 nm). Grids were stored in liquid nitrogen until imaging.

Cryo-ET data collection

Tilt series were collected on a 300-kV Titan Krios transmission electron microscope equipped with a Selectris energy filter and a Falcon4i detector (Thermo Fisher Scientific). Images were recorded at a nominal magnification of 64,000× in counting mode using Tomo5 (Thermo Fisher Scientific). The calibrated pixel size was 2 Å. For each tilt series, images were acquired using a modified dose-symmetric scheme (*47*) over a tilt range of -48° to +48° relative to the lamella, with 3° steps. At each tilt, images were recorded as movies of eight subframes. The cumulative electron dose per tilt series was ~150 $e^-/Å^2$. Defocus was set between −2.0 and −4.0 μm.

Tomogram reconstruction

Preprocessing, including motion correction, CTF estimation, and tilt-series generation, was performed in Warp 2 (*48*). Raw images were imported in Warp and processed by *WarpTools fs_motion_and_ctf*. Preprocessed raw images were imported as tilt series and visually examined in IMOD (*49*). Low-quality frames, including those obstructed by the stage, containing apparent crystalline ice, or displaying apparent jumps, were removed to generate new sets of tilt series in Warp. Selected tilt series were aligned automatically using AreTomo (*50*) within Warp. High-quality tilt series with TZ features were reconstructed into 6× binned tomograms at a pixel size of 12 Å in Warp.

Tomograms used for Fig. 1 were re-processed with MisAlignment (*51*) for tilt-series alignment, followed by tomogram reconstruction and Fourier filtering prior to visualization.

Tomogram segmentation

Six-times binned tomograms were imported into Amira (Thermo Fisher Scientific) for segmentation. A machine-learning model for membranes and ciliary-necklace densities was trained using manually selected targets and background regions chosen from tomogram slices. The resulting training set was used to generate a predictive model that was applied to tomograms for automatic segmentation. Segmentations were optimized by removing small, disconnected regions and applying median filtering to reduce noise.

Microtubules were segmented independently using TARDIS (https://github.com/SMLC-NYSBC/TARDIS) and imported into Amira. Microtubules that were not recognized by TARDIS were traced manually within Amira. Traces and nodes of segmented microtubules were automatically extracted using the Auto Skeleton module in Amira, then

Downloaded from https://www.science.org at Cornell University on September 14, 2026

further optimized using the Filament module to remove incorrect traces and intermediate nodes. Segmentation results were rendered in Amira.

Subtomogram averaging

From a total of 380 tomograms, ~250 exhibited visible TZ DMTs. Particle picking was performed on 209 tomograms using IMOD (*49*). For each TZ microtubule, points were manually placed along the DMT centerline, guided by cross-sectional slice views. Each set of picked points was saved as a separate *.mod* file. To maximize particle yield, particles were placed at 4-nm intervals along each centerline using *addModPts*. The *.mod* files were converted to coordinates using *model2point*, then to Warp-compatible *.star* files using *cryolo_boxmanager_tools.py* (*52*).

A total of 66,385 2× binned subtomograms were extracted along each TZ microtubule with 4-nm oversampling in Warp2 (*48*). The subtomograms were exported and aligned in RELION5 (*53*). Following alignment, all coordinates were manually inspected using Napari (*54*) and the ArtiaX plugin for ChimeraX (*55*), and misaligned particles were removed. To obtain the 8-nm TZ DMT repeat, 3D classification was performed with a generous mask covering the inner junction. After classification, well-aligned TZ particles were imported back to Warp/M to perform M refine. Refined particles were re-extracted with a pixel size of 2 Å/pixel and duplicated particles arising from oversampling were excluded. Then, the 33,196 8-nm particles were exported to RELION5. Local 3D classification and protofilament refinement were performed to improve MIP densities and microtubule-bound TZ linker densities, following strategies successful for axonemal DMTs (*56*, *57*).

For TZ linker analysis, coordinates of 66,385 particles with 4-nm interval were shifted to the center of the linker. 3D classifications on the linker and its adjacent protofilament using a generous local cylindrical mask resulted in 37,021 particles with linker density. Further 3D classifications and refinements were performed using tight masks to improve local resolution.

Local resolution was estimated using ResMap (*58*). The resulting local-resolution estimations were then projected onto the corresponding map surface and displayed as a color gradient in ChimeraX, with a fixed contour level and consistent color scale for visualization.

To analyze changes in the MIP repertoire during the transition from TZ to axonemal DMTs, we analyzed distal TZ particles that lacked TZ linker density (fig. S7C). Distal TZ DMTs were manually selected from tomograms and extracted with 4-nm oversampling, yielding 89,157 particles that were used to calculate an initial subtomogram average (fig. S7E). Masked classification focused on the inner junction was performed to isolate particles exhibiting 8-nm periodicity. Following removal of duplicates, 18,823 particles were retained. A subsequent round of masked classification was used to exclude particles containing TZ linker density. The remaining 7,341 particles were used to compute a reconstruction of distal TZ DMTs lacking TZ linkers (fig. S7F). The nominal resolution was 20 Å, as estimated using the 0.143 FSC criterion (fig. S7E).

During post-processing, the pixel size was changed from 2 Å to 1.924 Å to reflect more accurate microscope calibrations performed after data acquisition.

Domain recognition

DomainSeeker (*23*) was used to identify protein constituents in subtomogram averages. This computational tool fits domains from AlphaFold2-predicted structures to segmented density maps to assign the most probable domain to each region. Map segmentation was performed automatically using the Segment Map tool in ChimeraX (*59*, *60*). To construct a docking library, the entire predicted human proteome was downloaded from the AlphaFold Protein Structure Database (AFDB) (*61*) and subdivided into domains using a clique-based graph clustering algorithm informed by predicted aligned errors (PAE) from AlphaFold2. No prefiltering for structural redundancy was done; the only exclusions were proteins that exceeded the prediction capabilities of AlphaFold2 or domain groups containing fewer than 40 residues. The final screen contained 28,142 domains from 16,396 proteins. Each domain was fitted independently into the segmented densities and scored based on both overlap volume and Laplacian-filtered overlap correlation. Overlap volume measures the total volume of overlap between the fitted domain and the density map. Overlap correlation reports the cross-correlation computed after applying a Laplacian filter to the density map (which helps to sharpen the boundaries between protein features and solvent). To statistically assess the quality of the fit while accounting for size-dependent correlation bias, a local z-score metric was calculated, which measures how much each result deviates from the average correlation-volume relationship in two-dimensional space. Results were then ranked based on the local z-score. This approach successfully identified ECT2L and SKP1.

CFAP20 and CEP41 were assigned based on prior knowledge of DMT composition and did not require an unbiased screen, although CEP41 emerged as the best-fitting candidate when screening was performed (fig. S3A). CAPSL was identified as corresponding to the shelf-like densities in the TZ DMT by human-based fold recognition (fig. S4A). Visualization of these densities revealed multiple copies of a bilobal protein characterized by short α-helices, suggestive of EF-hand motifs. We hypothesized this density might correspond to a cilia-specific EF-hand-containing protein. To test this, we extracted a list of human proteins annotated as containing

Downloaded from https://www.science.org at Cornell University on September 14, 2026

EF-hands from UniProt (197 proteins; data S4) and filtered these based on their preferential localization to lung ciliated epithelial cells in single-cell RNA sequencing data (*26*). This filtering step yielded only seven proteins with strong, specific enrichment in multiciliated cells: CAPS, CAPSL, CETN2, CLXN, EFCAB11, EFCAB12 and EFHB. Structures of each of these proteins were predicted using AlphaFold3 (*62*) and Boltz-2 (*63*) and fitted to the density. CAPS and CAPSL gave plausible but suboptimal fits. To improve the fit, we used the experimentally determined structure of the *Tetrahymena thermophila* CAPS homolog, RIB22 (PDB: 8G3D) (*64*) as a template for homology modeling with SWISS-MODEL (*65*) and grafted a loop from this model onto the human CAPSL Boltz-2 model, resulting in an improved fit. To validate our final model, we ran DomainSeeker with the AlphaFold domain database supplemented with the atomic model of *T. thermophila* RIB22 and our optimized model of human CAPSL. The optimized model was the top-scoring solution (fig. S4B).

Model building and refinement

Atomic models were built in Coot (*66*). CFAP20 and α/β-tubulin models were obtained from PDB: 7UNG (*12*) and fit as rigid bodies into the subtomogram average. All other proteins were modeled using AlphaFold3 (*62*) or Boltz-2 (*63*) and fitted into the density either manually or using DomainSeeker. Low-confidence regions without supporting density were trimmed. To improve interfaces with the TZ linker array, three consecutive repeat units were assembled and refined jointly in Phenix using real-space refinement (*67*), with five macro-cycles of refinement, each consisting of global minimization with geometry restraints and rotamer and Ramachandran restraints to optimize sidechain conformations. Secondary structure was restrained to maintain hydrogen bonding patterns. After refinement, a single repeat unit of the TZ linker was retained for one further round of refinement. For the TZ DMT, initial atomic models were refined into the subtomogram averaging map using rigid-body refinement in phenix.real_space_refine. Geometry outliers were corrected manually for both TZ linker and DMT in Coot. Final refinement was performed in Phenix using group atomic displacement parameter (ADP) refinement against the subtomogram averages. Refined models were evaluated using map-model correlation and MolProbity (*68*) (table S1). In addition to the overall correlation, per-chain model-to-map correlation coefficients were obtained from Phenix and compiled for visualization (fig. S2, B and C).

Ultrastructure expansion microscopy (U-ExM)

Commercial MucilAir ALI cultures of human respiratory epithelium (Epithelix; batches MD0858 and MD0768) were maintained in 24-well plates containing 700 µL MucilAir culture medium per well at 37°C and 5% CO_2. Culture medium was replaced twice per week, and an apical mucus wash was performed once per week.

For U-ExM, an apical mucus wash was performed immediately before sample processing. One MucilAir insert was transferred to a 24-well plate containing 700 µL Dispase II (Roche, #04942078001; 5 U/mL in 1× PBS) and incubated for 15 min at 37°C to detach the tissue from the membrane. Tissue was then gently removed from the insert by pushing it off the membrane with a razor blade and transferred to the 10-mm microwell of a 35-mm glass-bottom dish (MatTek, #P35G-1.5-10-C). To increase the frequency of obtaining well-oriented cells for transverse imaging of the TZ, the two opposite ends of the MucilAir were folded toward the center.

The protocol was then performed as originally described, with slight modifications, from Gambarotto *et al.* (*69*). Samples were fixed overnight at 37°C in 1 mL of an anchoring solution containing 2% acrylamide and 1.4% formaldehyde in 1× PBS. The following day, the anchoring solution was replaced with 90 µL monomer solution (19% sodium acrylate, 0.1% bis-acrylamide and 10% acrylamide prepared in 10× PBS) and incubated for 30 min at room temperature (RT). The solution was then exchanged for 90 µL monomer solution supplemented with 0.5% tetramethylethylenediamine (TEMED) and 0.5% ammonium persulfate (APS), and a 24-mm coverslip was placed over the microwell to seal the chamber and initiate gelation, which proceeded for 15 min on ice followed by 1.5 hours at 37°C.

After polymerization, the coverslip was removed and the gel was trimmed around the tissue with a scalpel. The gel was then incubated in 1 mL denaturation buffer (200 mM sodium dodecyl sulfate, 200 mM NaCl, 50 mM Tris-HCl, pH 9) for 15 min at RT until it detached from the MatTek dish. The gel piece containing tissue was transferred to a 1.5-mL tube filled with fresh denaturation buffer and incubated for 1.5 hours at 95°C. The gel was then washed three times for 30 min in distilled water and manually sectioned with a razor blade to obtain transverse slices of ~0.5 mm thickness. Gel sections were stored at −20°C in 50% (v/v) glycerol.

For immunofluorescence analysis, selected gel sections were washed in three 15-min baths of distilled water, followed by two 15-min washes in PBS. Sections were incubated overnight at RT under gentle agitation with primary antibodies diluted in PBS containing 2% bovine serum albumin (PBS-BSA). After four 15-min washes in PBS with 0.1% Tween-20 (PBS-Tween), sections were incubated with secondary antibodies diluted in PBS-BSA for 2.5 hours at 37°C under agitation, followed by four additional 15-min washes in PBS-Tween. Gels were expanded by three successive 10-min incubations in distilled water. Expanded sections were mounted on 24-mm coverslips coated with poly-D-lysine (0.1 mg/mL) and imaged on an inverted Stellaris 8 confocal microscope

Downloaded from https://www.science.org at Cornell University on September 14, 2026

(Leica) using a 63×/1.4 NA oil-immersion objective with Lightning deconvolution.

The following primary antibodies were used for U-ExM: mouse monoclonal anti-α-tubulin (ABCD antibodies, #AA345; 1:400), mouse monoclonal anti-β-tubulin (ABCD antibodies, #AA344; 1:400), rabbit polyclonal anti-CAPS2 (Proteintech, #11924-1-AP; 1:250), rabbit polyclonal anti-CAPSL (Proteintech, #17174-1-AP; 1:250), rabbit polyclonal anti-DYNLL1 (Proteintech, #18130-1-AP; 1:250), rabbit polyclonal anti-DYNLL2 (Proteintech, #16811-1-AP; 1:250), rabbit polyclonal anti-DZANK1 (Atlas Antibodies, #HPA064255; 1:250), rabbit polyclonal anti-ENKD1 (Atlas Antibodies, #HPA041163; 1:250), rabbit polyclonal anti-ENKUR (Proteintech, #26440-1-AP; 1:250), rabbit polyclonal anti-MAP9 (Proteintech, #26078-1-AP; 1:250), and rabbit polyclonal anti-SKP1 (Proteintech, #10990-2-AP; 1:250).

U-ExM image analysis

Images were processed in FIJI (*70*). Measurements of the length and relative position of proteins of interest with respect to tubulin were carried out with the PickCentrioleDim plugin (*71*). Briefly, a line of equal length was drawn on each cilium selected for quantification (>20 cilia per protein), starting below the proximal end of the basal body and extending along the axoneme as defined by the tubulin signal. Intensity profiles for both tubulin and the protein of interest were extracted, and the start and end coordinates of each fluorescent signal were identified. The starting coordinate of the tubulin signal was set to 0, and the same shift was applied to the protein of interest. All corrected coordinates were exported to the CentrioleGraph plugin (*71*), which was used to generate plots illustrating the average relative position of each protein of interest with respect to tubulin.

For cross-sectional analyses, only TZs displaying circular tubulin and protein-of-interest signals were selected, thereby ensuring that no localization information was lost due to sample tilt. Images shown in the figures correspond either to a single optical section or to maximum-intensity projections of two consecutive z-planes.

The expansion factor (EF) was determined by measuring the width of 50 axonemes based on the tubulin signal and comparing these values to a reference axonemal width of 250 nm using PickCentrioleDim. The resulting mean EF (4.27) was used to correct all extracted measurements and to generate scale bars.

Genetic testing

Genomic DNA was extracted from peripheral blood samples using standard procedures. Whole-exome sequencing (WES) was performed at the Cologne Center for Genomics. Genomic DNA was enriched using Agilent SureSelect All Exon V6_r2 and SureSelect Whole Exome v7 capture kits (Agilent Technologies). Sequencing was performed on a HiSeq 2000 instrument (Illumina). Sequencing reads were mapped to the GRCh38 human reference genome. Variant analysis was performed using Varbank (https://varbank.ccg.uni-koeln.de/).

We analyzed a WES cohort of 489 individuals with suspected PCD (recurrent upper and lower airway infections) who lacked disease-causing variants in other known PCD genes. Variants were filtered based on population frequency, excluding those with a minor allele frequency (MAF) > 1% in gnomAD, dbSNP, or 1000 Genomes databases. Variant pathogenicity was assessed according to the guidelines of the American College of Medical Genetics and Genomics (ACMG) (*72*). Splice-site variants were evaluated using varSEAK (JSI Medical Systems; https://varseak.bio). *ECT2L* variants were confirmed by in-house Sanger sequencing using a 3730xl DNA Analyzer (Applied Biosystems). The trace files were analyzed using the CodonCode Aligner v.3.7.1. Segregation analysis was performed when parental and/or sibling DNA was available.

To analyze the effect of the splice-site variant c.2028+1_2028+18delinsTTTA on the transcript, RNA was isolated from ALI-cultured respiratory epithelial cells from a healthy control and individual OP-198 II1 (14 days after airlift) using the RNeasy Mini kit (Qiagen). PCR and sequencing were performed as described (*73*) using GoTaq Flexi DNA Polymerase (Promega).

Variant annotation for *ECT2L* and *DZANK1* was performed relative to the canonical Ensembl reference transcripts ENST00005541398.7 (*ECT2L*) and ENST00000699568.1 (*DZANK1*). In RNA-seq data from human airway epithelium we additionally detected an *ECT2L* isoform (ENST00000367682.6) that lacks the noncoding exon 2, and a *DZANK1* isoform (ENST00000699525.2) containing a shorter exon 6 that predicts an in-frame deletion of 19 amino acids. All variants reported in this study affected exons shared by the canonical and alternative isoforms.

Nasal nitric oxide (nNO) production rate measurements

Measurements of the nNO production rate were performed using an ANALYZER CLD 88 sp. instrument (Eco Medics) following the American Thoracic Society and European Respiratory Society (ERS/ATS) recommendations (*74*).

Human respiratory epithelial cells

Respiratory epithelial cells from individuals with suspected PCD were obtained by brushing the middle turbinate (Engelbrecht Medicine and Laboratory Technology). Cells were suspended in RPMI medium (Gibco, #11875093) supplemented with Antibiotic-Antimycotic (Gibco, #15240062). Cell suspensions were either used directly for downstream experiments or expanded under ALI conditions as described (*73*), with the

Downloaded from https://www.science.org at Cornell University on September 14, 2026

modification that Collagen Type I, rat tail (Corning, #354236) was used as a coating substrate.

Immunofluorescence microscopy of epithelial cells

Respiratory epithelial cells from nasal brushing or ALI cultures were spread onto glass slides, air-dried, and stored at −80°C until use. Two different staining protocols were used. Immunofluorescence staining with primary antibodies directed against IFT88 was performed as previously described (*73*) except the cells were blocked for 3–4 hours at RT, and the primary antibodies were incubated overnight at 4°C. All other immunofluorescence stainings were performed as follows. The cells were washed once with PBS and fixed with 4% paraformaldehyde for 30 min and with methanol/acetone (1:1) for 2 min (4°C). The cells were blocked overnight with 2% bovine serum albumin (BSA) diluted in 0.1% Triton X-100, before being incubated with the primary antibodies (for 3-4 hours at RT). After five washes with 0.1% Triton X-100 (5 min each), samples were incubated with secondary antibodies for 1 hour at RT. Primary and secondary antibodies were diluted in the blocking solution. DNA was stained with Hoechst 33342 (1:10,000 dilution; Sigma, #14533-100MG) for 15 min at RT, followed by five additional washes (5 min each) with 0.1% Triton X-100. Slides were mounted using DAKO fluorescent mounting medium (Dako North America). Confocal images were taken with a Zeiss LSM 880 laser scanning microscope using ZEN-black software and super-resolution microscopy images were taken with a Zeiss ELYRA 7 using ZEN-blue software (Carl Zeiss Microscopy). Final images were prepared with OMERO (*75*).

The following primary antibodies were used: monoclonal mouse anti-acetylated α-tubulin (1:10,000, Sigma Aldrich, #T6793), polyclonal rabbit anti-alpha/beta-tubulin (1:500, Cell Signaling Technology, #2148), polyclonal rabbit anti-ECT2L antibody (1:100, Atlas antibodies, #HPA035488), polyclonal rabbit anti-DZANK1 antibody (1:100, Atlas antibodies, #HPA064255), monoclonal mouse anti-NPHP1 (1:500; (*76*)), monoclonal mouse anti-CNTRL (1:200, Santa Cruz, #sc-365521), monoclonal mouse anti-SKP1 (1:100, Invitrogen, #32-3800) and polyclonal rabbit anti-IFT88 (1:100, Proteintech, #13967-1-AP).

The following secondary antibodies were used: Alexa Fluor 488-conjugated goat anti-mouse (1:1,000, Invitrogen, #A11029), Alexa Fluor 546-conjugated goat anti-rabbit (1:1,000, Invitrogen, #A11035), and Alexa Fluor 568-conjugated goat anti-rabbit (1:1,000; Invitrogen, #A11036).

Scanning electron microscopy (SEM) of ALI cultures

Fully differentiated ALI cultures were prepared for SEM using a modified osmium-thiocarbohydrazide-osmium (OTOTO) protocol (*77*). Cultures were fixed overnight in 2.5% glutaraldehyde and then washed five times for 10 min each in PBS. Samples were post-fixed in 1% (w/v) aqueous osmium tetroxide for 60 min, rinsed five times for 10 min each in distilled water, and incubated in the dark with 1% (w/v) aqueous thiocarbohydrazide for 20 min. After an additional water wash, the samples were incubated in 1% aqueous osmium tetroxide for 30 min. This thiocarbohydrazide-osmium sequence (water wash, 20-min thiocarbohydrazide incubation, water wash, 30-min osmium tetroxide incubation) was repeated once more and followed by a final water wash. Samples were dehydrated by graded ethanol incubations (30%, 50%, and 70%; 15 min each) and stored overnight in 70% ethanol at 4°C. The next day, samples were incubated for 30 min in 90% ethanol, followed by two 30-min incubations in 100% ethanol. Ethanol was substituted with liquid CO_2 by critical point drying (Leica EM CPD300; 20 replacement cycles). Dried samples were mounted on aluminum carriers using conductive carbon cement (Leit-C nach Goecke, Plano) and imaged with a Hitachi S-4700 field emission SEM (Hitachi Scientific Instruments) operated at 10 kV with secondary electron detection and a DISS5 digital scan generator (Point Electronic GmbH).

Transmission electron microscopy (TEM)

Freshly brushed respiratory epithelial cells or fully differentiated ALI cultures were processed for TEM using standard fixation and embedding protocols. Samples were fixed in 2.5% glutaraldehyde in Sørensen buffer overnight at 4°C, washed, and post-fixed in 1% osmium tetroxide. Following dehydration in a graded ethanol series, samples were incubated overnight at 4°C in a 1:2 mixture of 1,2-epoxypropane and Epon resin and subsequently embedded in Epon. After polymerization, ultrathin sections were cut, collected on copper grids, and contrasted with 8% (w/v) aqueous uranyl acetate and Reynolds' lead citrate. Sections were imaged using a Philips CM10 microscope equipped with a Quemesa camera (Olympus Soft Imaging Solutions) and iTEM SIS image acquisition software (Olympus Soft Imaging Solutions). In accordance with international consensus guidelines (*78*), >50 axonemal cross-sections from multiple cells were evaluated, including both proximal and distal ciliary regions. In addition, >50 TZ cross-sections were analyzed using dedicated series of sections targeted to this area.

High-speed video microscopy (HSVM) analysis

HSVM was performed according to ERS/ATS guidelines on two sample types: (i) native cells analyzed at 25 °C immediately after nasal brushing and (ii) cells obtained from ALI cultures analyzed at 37 °C after trypsinization. Samples were imaged using an inverted phase-contrast microscope (Nikon Eclipse Ti) equipped with a 63× objective and a digital high-speed video camera (Basler acA1300-200μm). Videos were recorded at a frame rate of 200 frames per second (fps).

Downloaded from https://www.science.org at Cornell University on September 14, 2026

Ciliary beat frequencies (CBFs) and ciliary beat patterns (CPBs) were analyzed using the Sisson-Ammons Video Analysis (SAVA) System (Ammons Engineering) (*79*). For movie S1, recordings were edited with FIJI/ImageJ v1.53c and labeled using Clipchamp (Microsoft).

In vitro ciliary transport assays

Ciliary transport assays (CTAs) were performed as described (*41*). Fluorescent 2-μm beads (FluoSpheres, Thermo Fisher Scientific) were added to the apical surface of fully differentiated (> 30 days) ALI cultures from OP-198 II1, OP-2226 II1, OP-3278 II1, and healthy controls. Particle motion was recorded at 37°C using a Leica THUNDER Imager (5× objective) with LAS-X software. CTAs were performed on seven inserts from two different brushings from OP-2226 II1, 12 inserts from OP-198 II1, and 15 inserts from OP-3278 II1. For each insert, 40 videos (from four field of views, with each recorded ten times) were acquired.

Particle trajectories were analyzed using NIS-Elements Advanced Research software (NIS-AR). To avoid edge artifacts, data within 0.5 mm of the insert border were excluded. To derive an averaged mean velocity representing the entire insert, each insert was divided into a regular 5×5 grid and the mean velocity of each grid cell was calculated. The average of the 25 means yields the representative velocity for each insert. The mean of all inserts was then calculated to derive the velocity of the culture. For statistical analysis, the mean velocities of all cultures from a single individual were combined (n = 3).

Phylogenetic and sequence analysis

Human protein sequences were retrieved from UniProt with the following accession numbers: CAPSL (Q8WWF8), DZANK1 (Q9NVP4), ECT2 (Q9H8V3), and ECT2L (Q008S8). For CAPSL paralogs, we used isoforms Q13938-4 (CAPS) and Q9BXY5-4 (CAPS2), which better agree with ribosomal profiling evidence (https://ribocrypt.org/) than canonical sequences.

Homologs were identified using Position-Specific Iterated BLAST (PSI-BLAST) against the NCBI database of non-redundant protein sequences. ECT2L homologs were defined as proteins containing both an F-box and a C-terminal DH–PH module. ECT2 homologs were defined as having N-terminal BRCT domains and a C-terminal DH–PH module. CAPSL and DZANK1 homologs were detected based on sequence similarity only without domain architecture constraints.

Species were selected to provide broad representation of eukaryotic diversity, including outgroups, while avoiding redundancy. Phylogenetic trees were generated from NCBI taxonomy identifiers using phyloT v2 (https://phylot.biobyte.de/) and visualized with iTOL v7 (https://itol.embl.de/) (*80*).

Protein domain schematics were generated using Protein Domain Designer (https://domaindesigner.farnunglab.com/). Sequence conservation was calculated using ConSurf (*81*). Protein sequence alignments were generated using ClustalOmega (*82*).

Gene expression visualization

Publicly available single-cell RNA sequencing (scRNA-seq) datasets were used to examine cell-type-specific gene expression patterns. Datasets were selected based on three criteria: (i) sufficient total cells for robust analysis, (ii) presence of multiciliated cells, and (iii) clear cell-type separation in UMAP visualization. Gene expression patterns were visualized using the built-in tools of each data portal and assessed qualitatively across cell populations.

Gene expression in lung tissues was analyzed using the Human Lung CellRef (v1.1) dataset, which aggregates 148 single-cell or single-nucleus RNA-seq datasets from 104 human lung donors, encompassing 505,256 cells (*26*). Data were accessed via the Human Lung CellRef ShinyCell browser: https://app.lungmap.net/app/shinycell-human-lung-cellref. Expression in the human fallopian tube was analyzed using a scRNA-seq dataset from four healthy, pre-menopausal individuals (59,738 cells) (*83*). Data were accessed via the CellxGene platform: https://cellxgene.cziscience.com/e/c6413315-7158-46c5-a5fd-7228385694f1.cxg/. Retinal gene expression was analyzed using a single-cell atlas of the adult human retina (244,474 cells) (*84*). Data were accessed via CellxGene: https://cellxgene.cziscience.com/e/0129dbd9-a7d3-4f6b-96b9-1da155a93748.cxg/. Expression in the brain was visualized using an integrated scRNA-seq atlas of the mouse brain (106,905 cells) (*85*). Mouse data were used due to the presence of an annotated ependymal cell population. Data were accessed via the Broad Institute Single Cell portal: https://singlecell.broadinstitute.org/single_cell/study/SCP3078/mcaoatlas-allcells.

AlphaFold-Multimer interaction screens

To identify potential binding partners of ECT2L and DZANK1, we performed pairwise structural prediction screens against a candidate list of 2,729 ciliary proteins (*5*). Target sequences were retrieved from UniProt, and pairwise multiple sequence alignments were generated using the MMseqs2 server (*86*). Structural predictions were performed with AlphaFold2-Multimer (v2.3.2) (*31*, *87*) via localcolabfold (v1.5.5) (*88*) on the O2 Compute Cluster at Harvard Medical School. Runs were configured with three recycles, five models per complex, and no templates. Compact Structure Prediction and Omics informed Classifier (cSPOC) scores (*89*) were calculated from the top three ranked predictions per complex. The predictions were sorted by descending cSPOC scores, with higher values indicating a greater likelihood of *bona fide*

Downloaded from https://www.science.org at Cornell University on September 14, 2026

interactions. The elbow point in the distribution of scores was detected using the KneeLocator algorithm (*90*) of the kneed (v0.8.5) python library. For targeted analysis of GTPase interactions with ECT2 and ECT2L, the screening library was restricted to Rho family GTPases rather than the full ciliary proteome.

Gene knockout

An *ECT2L* knockout (*ECT2L*-KO) was generated in human induced pluripotent stem cell (iPSC)-derived airway basal cells (iBCs) (*42*, *43*) using CRISPR-Cas9. Single-guide RNAs (sgRNAs) targeting the *ECT2L* locus were designed using CHOPCHOP (https://chopchop.cbu.uib.no/) (*91*). The selected crRNA sequences were: *5′*-AGGTGTCCAGGCACTAAATC-*3′* (*5′* site) and *5′*-GACGTTGCTTGTTAGTCCAG-*3′* (*3′* site). Cas9 nuclease (IDT, #1081060) and sgRNAs were delivered by nucleofection to a single-cell suspension of 10^5 iBCs in Primary Cell P3 solution (Lonza, #V4XP-3032). Nucleofected cells were grown in three-dimensional culture, where they formed clonal epithelial spheroids. Single spheroids were isolated manually, expanded, and screened to establish monoclonal populations. Screening was performed by PCR amplification and agarose gel electrophoresis to detect truncated amplicons; deletions were confirmed by sequencing. Successfully edited knockout clones were expanded and differentiated under ALI conditions. Wild-type control lines were generated in parallel using non-targeting sgRNAs lacking complementarity to the human genome.

Quantitative PCR (qPCR)

Total RNA was extracted from whole ALI inserts using the RNeasy Mini Kit (Qiagen, #74104) and reverse-transcribed into cDNA using TaqMan Reverse Transcription Reagents (Applied Biosystems, #N8080234). Quantitative PCR was performed on a QuantStudio 6 Flex system (Applied Biosystems) for 40 cycles using TaqMan Gene Expression Assays (Applied Biosystems) in technical triplicates. The following TaqMan probes targeting *ECT2L* were used: exon 5-6 (Hs01009598_m1) and exon 16 (Hs01009592_m1). Relative gene expression was calculated from the mean C_t of technical triplicates, normalized to 18S rRNA, and presented as fold change using the $2^{-\Delta\Delta Ct}$ method relative to NTCs (*92*). Assays with undetectable amplification were assigned a C_t value of 40.

Protein expression and pull-down assays

The gene fragment encoding human ECT2L or DZANK1 was synthesized (GenScript) and cloned into a pcDNA3.1 vector. ECT2L was engineered to contain an N-terminal His-tag followed by a 3×FLAG-tag and DZANK1 was engineered to contain an N-terminal 2xSTREP-tag.

For pull-down assays, Expi293F cells (Gibco, #A14527) were transfected using polyethylenimine (PEI; 3:1 PEI:DNA) under the following conditions: negative control (NC; no DNA), 0.1 mg pcDNA3.1-ECT2L (100 mL culture), 0.1 mg pcDNA3.1-DZANK1 (100 mL culture), or co-transfection with 0.1 mg pcDNA3.1-ECT2L plus 0.1 mg pcDNA3.1-DZANK1 (200 mL culture). After 48 hours, cells were harvested and resuspended in 20 mL lysis buffer (30 mM Tris-HCl, pH 7.8; 300 mM NaCl; 2 mM TCEP; 0.1% NP-40; 5% glycerol) supplemented with EDTA-free Complete protease inhibitor (Roche). Cells were sonicated on ice at 40% amplitude for 2 min (1 s on/6 s off) and clarified by centrifugation at 25,000 rpm for 1 hour at 4°C (Ti45 rotor; Beckman Optima L-90K).

Cleared lysates were incubated with 400 μL anti-FLAG M2 resin (Sigma, #A2220). After five washes, bound proteins were eluted with 400 μL lysis buffer containing 0.8 mg/mL 3×FLAG peptide (Sigma). A 40-μL aliquot of each eluate was reserved for subsequent immunoblot and mass spectrometry analyses. The ECT2L eluate was additionally concentrated for use as a positive control in subsequent immunoblot analyses.

Mass spectrometry results are provided as data S6. For quantitative comparisons (Fig. 4D), peptide intensities were first summed per protein and sample. For each protein, sample intensities were normalized by dividing each sample intensity (%) by the minimum nonzero intensity across the four conditions (minimum detected = 1). Samples with undetected signal were assigned a value of 0.

Immunoblot analysis

Immunoblotting was performed on three sample types: (i) pull-down eluates from transfected Expi293F cells, (ii) lysates from patient cells, and (iii) sequential protein extracts from ALI cultures of *ECT2L*-KO and wild-type non-targeting control (NTC) lines.

For patient samples, protein extraction and immunoblot analyses were performed as described (*93*). For ALI cultures of *ECT2L*-KO and wild-type non-targeting control (NTC) lines, Extracts 1 and 2 were obtained using the NE-PER Nuclear and Cytoplasmic Extraction Kit (Thermo Fisher Scientific, #78833) according to the manufacturer's instructions. To obtain Extract 3, the remaining pellet was resuspended in urea lysis buffer (50 mM Tris-HCl pH 7.5, 7.2 M urea, 2% SDS, and protease inhibitor cocktail; Cell Signaling Technology, #5871), mechanically disrupted by repeated passage through a syringe, incubated for 30 min at RT with intermittent vortexing, and centrifuged at 16,000 × *g* for 10 min. The supernatant was collected as Extract 3. Protein concentrations were determined using the Pierce BCA Protein Assay Kit (Thermo Fisher Scientific, #23225). For ALI extracts, 30 μg of Extract 1, 20 μg of Extract 2, and 30 μg of Extract 3 were loaded.

Proteins were separated by SDS-PAGE on Bolt 4-12% Bis-

Downloaded from https://www.science.org at Cornell University on September 14, 2026

Tris gels (Invitrogen, #NW04120) and transferred to Immobilon-FL PVDF membranes (Millipore, #IPFL00010). Membranes were blocked for 1 hour at RT with Intercept Blocking Buffer (LI-COR Biosciences, #927-60001) or 5% skim milk (MP Biomedicals, #908827) and incubated overnight at 4°C with primary antibodies diluted in blocking buffer. Primary antibodies used were: mouse anti-strep (1:2000, Sigma-Aldrich, #SAB2702216), rabbit anti-ECT2L (1:1,000, Novus Biologicals, #NBP1-90847), polyclonal rabbit anti-DZANK1 antibody (1:100, #HPA064255), mouse anti-GAPDH (1:10,000, Fitzgerald Industries, #10R-G109a), and mouse anti-acetylated α-tubulin (1:1,000, Sigma-Aldrich, #T7451). After washing, membranes were incubated for 1 hour at RT with near-infrared fluorescent secondary antibodies (1:5,000, LI-COR Biosciences): IRDye 800CW goat anti-rabbit IgG (#926-32211) or IRDye 680LT goat anti-mouse IgG (#926-68020) or HRP goat anti-mouse IgG (Thermo Fisher Scientific, #311430), HRP goat anti-rabbit IgG (Thermo Fisher Scientific, #311460). Signals were detected using an Odyssey CLx Imaging System (LI-COR Biosciences) or ChemiDoc Imaging System (Bio-Rad).

Electron microscopy analysis of ECT2L-*KO cells*

For TEM, fully differentiated ALI cultures were fixed in a primary fixative containing 2.5% glutaraldehyde, 1.25% paraformaldehyde, and 0.03% picric acid in 0.1 M sodium cacodylate buffer (pH 7.4) at RT for at least 1 hour. Samples were post-fixed for 30 min at RT in 1% osmium tetroxide and 1.5% potassium ferrocyanide in distilled water, rinsed three times in distilled water, and incubated for 30 min in 1% (w/v) aqueous uranyl acetate. After two additional water rinses, samples were dehydrated through a graded ethanol series (50%, 70%, 95%, and 2 × 100%; 5 min each). Membranes were then excised from the plastic supports, cut into strips in 100% ethanol, and incubated in propylene oxide for 30 min. Samples were infiltrated overnight at RT in a 1:1 mixture of propylene oxide and TAAB Epon resin (TAAB Laboratories Equipment Ltd.) and subsequently embedded in fresh TAAB Epon. Polymerization was carried out at 60°C for 48 hours. Ultrathin sections (~60 nm) were cut on a Reichert Ultracut-S ultramicrotome, collected on copper grids, and stained with lead citrate. Sections were examined with a JEOL 1200EX transmission electron microscope, and images were acquired with an AMT 2k CCD camera.

For SEM, fully differentiated ALI cultures were fixed for 1–2 hours at RT in 2% glutaraldehyde and 2.5% formaldehyde in 0.1 M sodium cacodylate buffer (pH 7.4). Following fixation, specimens were rinsed three times in 0.1 M sodium cacodylate buffer (pH 7.4) for 10–15 min each and post-fixed for 1–2 hours at RT in 1% osmium tetroxide in the same buffer. Samples were rinsed three times for 5 min each in 0.1 M sodium cacodylate buffer, dehydrated through a graded ethanol series (35%, 50%, 70%, 80%, 95%, and 2 × 100%; 5, 5, 5, 10, 10, and 10 min, respectively), and subjected to critical-point drying for 45-60 min. Dried specimens were mounted on aluminum stubs and sputter-coated with a 1-2 nm conductive metal layer. Images were acquired with a Hitachi S-4700 field emission SEM (Hitachi High-Technologies).

Statistical analysis

Statistical analyses were performed using GraphPad Prism v10. For the ciliary transport assay, statistical significance was assessed using a Mann-Whitney U test comparing cultures from *ECT2L*- and *DZANK1*-individuals (n = 3) to cultures from healthy control individuals (n = 19). For RT-qPCR, statistical significance was assessed by unpaired two-tailed *t* test. Sample sizes (n) and P values for each experiment are reported in the corresponding figure legends. No statistical methods were used to predetermine sample sizes. Experiments were not randomized, and investigators were not blinded to experimental conditions during data collection and analysis.

REFERENCES AND NOTES

1. A. L. Moran, L. Louzao-Martinez, D. P. Norris, D. J. M. Peters, O. E. Blacque, Transport and barrier mechanisms that regulate ciliary compartmentalization and ciliopathies. *Nat. Rev. Nephrol.* **20**, 83–100 (2024). doi:10.1038/s41581-023-00773-2 Medline
2. H. Long, K. Huang, Transport of ciliary membrane proteins. *Front. Cell Dev. Biol.* **7**, 381 (2020). doi:10.3389/fcell.2019.00381 Medline
3. S. R. Shinde, A. R. Nager, M. V. Nachury, Ubiquitin chains earmark GPCRs for BBSome-mediated removal from cilia. *J. Cell Biol.* **219**, e202003020 (2020). doi:10.1083/jcb.202003020 Medline
4. P. B. Desai, M. W. Stuck, B. Lv, G. J. Pazour, Ubiquitin links smoothened to intraflagellar transport to regulate Hedgehog signaling. *J. Cell Biol.* **219**, e201912104 (2020). doi:10.1083/jcb.201912104 Medline
5. S. M. Lange, J. A. Bennett, R. J. Eisert, A. Brown, A conserved mechanism for the retrieval of polyubiquitinated proteins from cilia. *Cell* **188**, 6492–6508.e18 (2025). doi:10.1016/j.cell.2025.07.043 Medline
6. G. A. Greenan, R. D. Vale, D. A. Agard, Electron cryotomography of intact motile cilia defines the basal body to axoneme transition. *J. Cell Biol.* **219**, e201907060 (2020). doi:10.1083/jcb.201907060 Medline
7. J. C. Van De Weghe, A. Gomez, D. Doherty, The Joubert-Meckel-nephronophthisis spectrum of ciliopathies. *Annu. Rev. Genomics Hum. Genet.* **23**, 301–329 (2022). doi:10.1146/annurev-genom-121321-093528 Medline
8. K. A. Despotes, M. A. Zariwala, S. D. Davis, T. W. Ferkol, Primary ciliary dyskinesia: A clinical review. *Cells* **13**, 974 (2024). doi:10.3390/cells13110974 Medline
9. N. B. Gilula, P. Satir, The ciliary necklace. A ciliary membrane specialization. *J. Cell Biol.* **53**, 494–509 (1972). doi:10.1083/jcb.53.2.494 Medline
10. S. Ma, L. Li, Z. Li, S. Luo, Q. Liu, W. Du, B. Qiu, M. Gui, X. Zhu, Q. Guo, In situ cryo-electron tomography reveals the progressive biogenesis of basal bodies and cilia in mouse ependymal cells. *Nat. Commun.* **16**, 5932 (2025). doi:10.1038/s41467-025-61015-6 Medline
11. H. van den Hoek, N. Klena, M. A. Jordan, G. Alvarez Viar, R. D. Righetto, M. Schaffer, P. S. Erdmann, W. Wan, S. Geimer, J. M. Plitzko, W. Baumeister, G. Pigino, V. Hamel, P. Guichard, B. D. Engel, In situ architecture of the ciliary base reveals the stepwise assembly of intraflagellar transport trains. *Science* **377**, 543–548 (2022). doi:10.1126/science.abm6704 Medline
12. M. Gui, J. T. Croft, D. Zabeo, V. Acharya, J. M. Kollman, T. Burgoyne, J. L. Höög, A. Brown, SPACA9 is a lumenal protein of human ciliary singlet and doublet microtubules. *Proc. Natl. Acad. Sci. U.S.A.* **119**, e2207605119 (2022). doi:10.1073/pnas.2207605119 Medline
13. T. Walton, M. Gui, S. Velkova, M. R. Fassad, R. A. Hirst, E. Haarman, C. O'Callaghan,

Downloaded from https://www.science.org at Cornell University on September 14, 2026

M. Bottier, T. Burgoyne, H. M. Mitchison, A. Brown, Axonemal structures reveal mechanoregulatory and disease mechanisms. *Nature* **618**, 625–633 (2023). doi:10.1038/s41586-023-06140-2 Medline
14. B. Setu, Q. Nie, G. Echele, S. A. Spencer, Calcyphosine is a microtubule-associated protein required for spindle formation and function. bioRxiv 573632 [Preprint] (2024); https://doi.org/10.1101/2023.12.29.573632.
15. H. Dong, X. Li, Z. Lou, X. Xu, D. Su, X. Zhou, W. Zhou, M. Bartlam, Z. Rao, Crystal-structure and biochemical characterization of recombinant human calcyphosine delineates a novel EF-hand-containing protein family. *J. Mol. Biol.* **383**, 455–464 (2008). doi:10.1016/j.jmb.2008.08.048 Medline
16. S. P. Choksi, D. Babu, D. Lau, X. Yu, S. Roy, Systematic discovery of novel ciliary genes through functional genomics in the zebrafish. *Development* **141**, 3410–3419 (2014). doi:10.1242/dev.108209 Medline
17. B. Cetin, A. Taheri, M. Golcuk, B. Y. Monroy, J. Fernandes, K. M. Ori-McKenney, M. Gur, E. Nogales, A. Yildiz, Structure and mechanism of microtubule stabilization and motor regulation by MAP9. bioRxiv 688911 [Preprint] (2025); https://doi.org/10.1101/2025.11.17.688911.
18. M. V. Tran, D. Khuntsariya, R. D. Fetter, J. W. Ferguson, J. T. Wang, A. F. Long, L. E. Cote, S. R. Wellard, N. Vázquez-Martínez, M. D. Sallee, M. Genova, M. M. Magiera, S. Eskinazi, J. D. Lee, N. Peel, C. Janke, T. Stearns, K. Shen, Z. Lansky, J. Magescas, J. L. Feldman, MAP9/MAPH-9 supports axonemal microtubule doublets and modulates motor movement. *Dev. Cell* **59**, 199–210.e11 (2024). doi:10.1016/j.devcel.2023.12.001 Medline
19. R. G. Das, F. P. Marinho, S. Iwabe, E. Santana, K. S. McDaid, G. D. Aguirre, K. Miyadera, Variabilities in retinal function and structure in a canine model of cone-rod dystrophy associated with RPGRIP1 support multigenic etiology. *Sci. Rep.* **7**, 12823 (2017). doi:10.1038/s41598-017-13112-w Medline
20. K. Takahashi, J. C. Kwok, Y. Sato, G. D. Aguirre, K. Miyadera, Molecular characterization of MAP9 in the photoreceptor sensory cilia as a modifier in canine *RPGRIP1*-associated cone-rod dystrophy. *Front. Cell. Neurosci.* **17**, 1226603 (2023). doi:10.3389/fncel.2023.1226603 Medline
21. J.-M. Saffin, M. Venoux, C. Prigent, J. Espeut, F. Poulat, D. Giorgi, A. Abrieu, S. Rouquier, ASAP, a human microtubule-associated protein required for bipolar spindle assembly and cytokinesis. *Proc. Natl. Acad. Sci. U.S.A.* **102**, 11302–11307 (2005). doi:10.1073/pnas.0500964102 Medline
22. B. Y. Monroy, T. C. Tan, J. M. Oclaman, J. S. Han, S. Simó, S. Niwa, D. W. Nowakowski, R. J. McKenney, K. M. Ori-McKenney, A Combinatorial MAP Code Dictates Polarized Microtubule Transport. *Dev. Cell* **53**, 60–72.e4 (2020). doi:10.1016/j.devcel.2020.01.029 Medline
23. Y. Lu, G. Chen, F. Sun, Y. Zhu, Z. Zhang, De novo identification of protein domains in cryo-electron tomography maps from AlphaFold2 models. bioRxiv 623534 (2024); https://doi.org/10.1101/2024.11.21.623534.
24. T. Miki, C. L. Smith, J. E. Long, A. Eva, T. P. Fleming, Oncogene ect2 is related to regulators of small GTP-binding proteins. *Nature* **362**, 462–465 (1993). doi:10.1038/362462a0 Medline
25. GTEx Consortium, The Genotype-Tissue Expression (GTEx) project. *Nat. Genet.* **45**, 580–585 (2013). doi:10.1038/ng.2653 Medline
26. M. Guo, M. P. Morley, C. Jiang, Y. Wu, G. Li, Y. Du, S. Zhao, A. Wagner, A. C. Cakar, M. Kouril, K. Jin, N. Gaddis, J. A. Kitzmiller, K. Stewart, M. C. Basil, S. M. Lin, Y. Ying, A. Babu, K. A. Wikenheiser-Brokamp, K. S. Mun, A. P. Naren, G. Clair, J. N. Adkins, G. S. Pryhuber, R. S. Misra, B. J. Aronow, T. L. Tickle, N. Salomonis, X. Sun, E. E. Morrisey, J. A. Whitsett, NHLBI LungMAP Consortium, S. Lin, Y. Xu, Guided construction of single cell reference for human and mouse lung. *Nat. Commun.* **14**, 4566 (2023). doi:10.1038/s41467-023-40173-5 Medline
27. K. Yan, Z. Zhang, J. Yang, S. H. McLaughlin, D. Barford, Architecture of the CBF3-centromere complex of the budding yeast kinetochore. *Nat. Struct. Mol. Biol.* **25**, 1103–1110 (2018). doi:10.1038/s41594-018-0154-1 Medline
28. J.-M. Galan, A. Wiederkehr, J. H. Seol, R. Haguenauer-Tsapis, R. J. Deshaies, H. Riezman, M. Peter, Skp1p and the F-box protein Rcy1p form a non-SCF complex involved in recycling of the SNARE Snc1p in yeast. *Mol. Cell. Biol.* **21**, 3105–3117 (2001). doi:10.1128/MCB.21.9.3105-3117.2001 Medline
29. K. L. Rossman, C. J. Der, J. Sondek, GEF means go: Turning on RHO GTPases with guanine nucleotide-exchange factors. *Nat. Rev. Mol. Cell Biol.* **6**, 167–180 (2005). doi:10.1038/nrm1587 Medline
30. T. Tatsumoto, X. Xie, R. Blumenthal, I. Okamoto, T. Miki, Human ECT2 is an exchange factor for Rho GTPases, phosphorylated in G2/M phases, and involved in cytokinesis. *J. Cell Biol.* **147**, 921–928 (1999). doi:10.1083/jcb.147.5.921 Medline
31. R. Evans, M. O'Neill, A. Pritzel, N. Antropova, A. Senior, T. Green, A. Žídek, R. Bates, S. Blackwell, J. Yim, O. Ronneberger, S. Bodenstein, M. Zielinski, A. Bridgland, A. Potapenko, A. Cowie, K. Tunyasuvunakool, R. Jain, E. Clancy, P. Kohli, J. Jumper, D. Hassabis, Protein complex prediction with AlphaFold-Multimer. bioRxiv 463034 [Preprint] (2021); https://doi.org/10.1101/2021.10.04.463034.
32. M. Dona, R. Bachmann-Gagescu, Y. Texier, G. Toedt, L. Hetterschijt, E. L. Tonnaer, T. A. Peters, S. E. C. van Beersum, J. G. M. Bergboer, N. Horn, E. de Vrieze, R. W. N. Slijkerman, J. van Reeuwijk, G. Flik, J. E. Keunen, M. Ueffing, T. J. Gibson, R. Roepman, K. Boldt, H. Kremer, E. van Wijk, NINL and DZANK1 co-function in vesicle transport and are essential for photoreceptor development in zebrafish. *PLOS Genet.* **11**, e1005574 (2015). doi:10.1371/journal.pgen.1005574 Medline
33. A. Shoemark, M. Goutaki, B. Kinghorn, C. Ardura-Garcia, N. Baz-Redón, M. Chilvers, S. D. Davis, J. De Brandt, S. Dell, R. Dhar, L. Dixon, T. Ferkol, C. Hogg, M. Legendre, M. Leigh, J. S. Lucas, M. Manion, N. Rumman, I. Toews, V. Labonte, W. B. Wee, P. Kouis, A. Horani, European Respiratory Society and American Thoracic Society guidelines for the diagnosis of primary ciliary dyskinesia. *Eur. Respir. J.* **66**, 2500745 (2025). doi:10.1183/13993003.00745-2025 Medline
34. C. Huber, S. Wu, A. S. Kim, S. Sigaudy, A. Sarukhanov, V. Serre, G. Baujat, K.-H. Le Quan Sang, D. L. Rimoin, D. H. Cohn, A. Munnich, D. Krakow, V. Cormier-Daire, WDR34 mutations that cause short-rib polydactyly syndrome type III/severe asphyxiating thoracic dysplasia reveal a role for the NF-κB pathway in cilia. *Am. J. Hum. Genet.* **93**, 926–931 (2013). doi:10.1016/j.ajhg.2013.10.007 Medline
35. L. Vuolo, N. L. Stevenson, K. J. Heesom, D. J. Stephens, Dynein-2 intermediate chains play crucial but distinct roles in primary cilia formation and function. *eLife* **7**, e39655 (2018). doi:10.7554/eLife.39655 Medline
36. A. E. Merrill, B. Merriman, C. Farrington-Rock, N. Camacho, E. T. Sebald, V. A. Funari, M. J. Schibler, M. H. Firestein, Z. A. Cohn, M. A. Priore, A. K. Thompson, D. L. Rimoin, S. F. Nelson, D. H. Cohn, D. Krakow, Ciliary abnormalities due to defects in the retrograde transport protein DYNC2H1 in short-rib polydactyly syndrome. *Am. J. Hum. Genet.* **84**, 542–549 (2009). doi:10.1016/j.ajhg.2009.03.015 Medline
37. K. Kessler, I. Wunderlich, S. Uebe, N. S. Falk, A. Gießl, J. H. Brandstätter, B. Popp, P. Klinger, A. B. Ekici, H. Sticht, H.-G. Dörr, A. Reis, R. Roepman, E. Seemanová, C. T. Thiel, DYNC2LI1 mutations broaden the clinical spectrum of dynein-2 defects. *Sci. Rep.* **5**, 11649 (2015). doi:10.1038/srep11649 Medline
38. W. Fu, L. Wang, S. Kim, J. Li, B. D. Dynlacht, Role for the IFT-A complex in selective transport to the primary cilium. *Cell Rep.* **17**, 1505–1517 (2016). doi:10.1016/j.celrep.2016.10.018 Medline
39. T. Hirano, Y. Katoh, K. Nakayama, Intraflagellar transport-A complex mediates ciliary entry and retrograde trafficking of ciliary G protein-coupled receptors. *Mol. Biol. Cell* **28**, 429–439 (2017). doi:10.1091/mbc.e16-11-0813 Medline
40. M. M. Oud, C. Bonnard, D. A. Mans, U. Altunoglu, S. Tohari, A. Y. J. Ng, A. Eskin, H. Lee, C. A. Rupar, N. P. de Wagenaar, K. M. Wu, P. Lahiry, G. J. Pazour, S. F. Nelson, R. A. Hegele, R. Roepman, H. Kayserili, B. Venkatesh, V. M. Siu, B. Reversade, H. H. Arts, A novel ICK mutation causes ciliary disruption and lethal endocrine-cerebro-osteodysplasia syndrome. *Cilia* **5**, 8 (2016). doi:10.1186/s13630-016-0029-1 Medline
41. K. Wohlgemuth, N. Hoersting, J. Koenig, N. T. Loges, J. Raidt, S. George, S. Cindrić, A. Schramm, L. Biebach, S. Lay, G. W. Dougherty, H. Olbrich, P. Pennekamp, B. Dworniczak, H. Omran, Pathogenic variants in *CFAP46*, *CFAP54*, *CFAP74* and *CFAP221* cause primary ciliary dyskinesia with a defective C1d projection of the central apparatus. *Eur. Respir. J.* **64**, 2400790 (2024). doi:10.1183/13993003.00790-2024 Medline
42. F. J. Hawkins, S. Suzuki, M. L. Beermann, C. Barillà, R. Wang, C. Villacorta-Martin, A. Berical, J. C. Jean, J. Le Suer, T. Matte, C. Simone-Roach, Y. Tang, T. M. Schlaeger, A. M. Crane, N. Matthias, S. X. L. Huang, S. H. Randell, J. Wu, J. R. Spence, G. Carraro, B. R. Stripp, A. Rab, E. J. Sorsher, A. Horani, S. L. Brody, B. R. Davis, D. N. Kotton, Derivation of airway basal stem cells from human pluripotent stem cells. *Cell Stem Cell* **28**, 79–95.e8 (2021). doi:10.1016/j.stem.2020.09.017 Medline
43. A. C. Berical, H. Kiyokawa, M. L. Beermann, D. Wallman, G. Cherfane, V. Dunphy, J. Pan, A. Tilston-Lunel, X. Varelas, A. Horani, S. L. Brody, D. N. Kotton, F. J. Hawkins, Airway disease modeling with gene-edited human basal cell

Downloaded from https://www.science.org at Cornell University on September 14, 2026

transplantation. *Am. J. Respir. Crit. Care Med.* **211**, 131–134 (2025). doi:10.1164/rccm.202406-1110RL Medline
44. L. Stepanek, G. Pigino, Microtubule doublets are double-track railways for intraflagellar transport trains. *Science* **352**, 721–724 (2016). doi:10.1126/science.aaf4594 Medline
45. O. Mercey, C. Kostic, E. Bertiaux, A. Giroud, Y. Sadian, D. C. A. Gaboriau, C. G. Morrison, N. Chang, Y. Arsenijevic, P. Guichard, V. Hamel, The connecting cilium inner scaffold provides a structural foundation that protects against retinal degeneration. *PLOS Biol.* **20**, e3001649 (2022). doi:10.1371/journal.pbio.3001649 Medline
46. H. Park, M. Choi, Y. Zhang, H. O.-L. Cheung, S. Makino, Y. Yoshikawa, H. Qi, Z. Liu, G. Lan, G. Fu, Q. Wang, S. S. Guo, P. Liu, Z. Liu, S.-C. Ti, W.-J. Wang, X. D. Li, T. Ni, C.-C. Hui, M. He, The kinesin-4 protein KIF27 forms a cytoskeletal scaffold at the transition zone to promote motile cilia structural integrity. *Proc. Natl. Acad. Sci. U.S.A.* **122**, e2515392122 (2025). doi:10.1073/pnas.2515392122 Medline
47. W. J. H. Hagen, W. Wan, J. A. G. Briggs, Implementation of a cryo-electron tomography tilt-scheme optimized for high resolution subtomogram averaging. *J. Struct. Biol.* **197**, 191–198 (2017). doi:10.1016/j.jsb.2016.06.007 Medline
48. D. Tegunov, P. Cramer, Real-time cryo–EM data pre-processing with Warp. *Nat. Methods* **16**, 1146–1152 (2019). doi:10.1038/s41592-019-0580-y Medline
49. J. R. Kremer, D. N. Mastronarde, J. R. McIntosh, Computer visualization of three-dimensional image data using IMOD. *J. Struct. Biol.* **116**, 71–76 (1996). doi:10.1006/jsbi.1996.0013 Medline
50. S. Zheng, G. Wolff, G. Greenan, Z. Chen, F. G. A. Faas, M. Bárcena, A. J. Koster, Y. Cheng, D. A. Agard, AreTomo: An integrated software package for automated marker-free, motion-corrected cryo-electron tomographic alignment and reconstruction. *J. Struct. Biol. X* **6**, 100068 (2022). doi:10.1016/j.yjsbx.2022.100068 Medline
51. M. L. Chaillet, J. van Loenhout, M. R. Leung, A. Burt, D. Tegunov, MissAlignment teaches itself better cryo-ET tilt-series alignment by making it worse. bioRxiv 721716 (2026); https://doi.org/10.64898/2026.04.29.721716.
52. T. Wagner, F. Merino, M. Stabrin, T. Moriya, C. Antoni, A. Apelbaum, P. Hagel, O. Sitsel, T. Raisch, D. Prumbaum, D. Quentin, D. Roderer, S. Tacke, B. Siebolds, E. Schubert, T. R. Shaikh, P. Lill, C. Gatsogiannis, S. Raunser, SPHIRE-crYOLO is a fast and accurate fully automated particle picker for cryo-EM. *Commun. Biol.* **2**, 218–13 (2019). doi:10.1038/s42003-019-0437-z Medline
53. A. Burt, B. Toader, R. Warshamanage, A. von Kügelgen, E. Pyle, J. Zivanov, D. Kimanius, T. A. M. Bharat, S. H. W. Scheres, An image processing pipeline for electron cryo-tomography in RELION-5. *FEBS Open Bio* **14**, 1788–1804 (2024). doi:10.1002/2211-5463.13873 Medline
54. C.-L. Chiu, N. Clack, The napari Community, napari: A python multi-dimensional image viewer platform for the research community. *Microsc. Microanal.* **28**, 1576–1577 (2022). doi:10.1017/S1431927622006328
55. U. H. Ermel, S. M. Arghittu, A. S. Frangakis, X. Artia, An electron tomography toolbox for the interactive handling of sub-tomograms in UCSF ChimeraX. *Protein Sci.* **31**, e4472 (2022). doi:10.1002/pro.4472 Medline
56. M. Ma, M. Stoyanova, G. Rademacher, S. K. Dutcher, A. Brown, R. Zhang, Structure of the decorated ciliary doublet microtubule. *Cell* **179**, 909–922.e12 (2019). doi:10.1016/j.cell.2019.09.030 Medline
57. T. Walton, M. H. Doran, A. Brown, Structural determination and modeling of ciliary microtubules. *Acta Crystallogr. D Struct. Biol.* **80**, 220–231 (2024). doi:10.1107/S2059798324001815 Medline
58. A. Kucukelbir, F. J. Sigworth, H. D. Tagare, Quantifying the local resolution of cryo-EM density maps. *Nat. Methods* **11**, 63–65 (2014). doi:10.1038/nmeth.2727 Medline
59. E. C. Meng, T. D. Goddard, E. F. Pettersen, G. S. Couch, Z. J. Pearson, J. H. Morris, T. E. Ferrin, UCSF ChimeraX: Tools for structure building and analysis. *Protein Sci.* **32**, e4792 (2023). doi:10.1002/pro.4792 Medline
60. G. D. Pintilie, J. Zhang, T. D. Goddard, W. Chiu, D. C. Gossard, Quantitative analysis of cryo-EM density map segmentation by watershed and scale-space filtering, and fitting of structures by alignment to regions. *J. Struct. Biol.* **170**, 427–438 (2010). doi:10.1016/j.jsb.2010.03.007 Medline
61. M. Varadi, S. Anyango, M. Deshpande, S. Nair, C. Natassia, G. Yordanova, D. Yuan, O. Stroe, G. Wood, A. Laydon, A. Žídek, T. Green, K. Tunyasuvunakool, S. Petersen, J. Jumper, E. Clancy, R. Green, A. Vora, M. Lutfi, M. Figurnov, A. Cowie, N. Hobbs, P. Kohli, G. Kleywegt, E. Birney, D. Hassabis, S. Velankar, AlphaFold Protein Structure Database: Massively expanding the structural coverage of protein-sequence space with high-accuracy models. *Nucleic Acids Res.* **50**, D439–D444 (2022). doi:10.1093/nar/gkab1061 Medline
62. J. Abramson, J. Adler, J. Dunger, R. Evans, T. Green, A. Pritzel, O. Ronneberger, L. Willmore, A. J. Ballard, J. Bambrick, S. W. Bodenstein, D. A. Evans, C.-C. Hung, M. O'Neill, D. Reiman, K. Tunyasuvunakool, Z. Wu, A. Žemgulytė, E. Arvaniti, C. Beattie, O. Bertolli, A. Bridgland, A. Cherepanov, M. Congreve, A. I. Cowen-Rivers, A. Cowie, M. Figurnov, F. B. Fuchs, H. Gladman, R. Jain, Y. A. Khan, C. M. R. Low, K. Perlin, A. Potapenko, P. Savy, S. Singh, A. Stecula, A. Thillaisundaram, C. Tong, S. Yakneen, E. D. Zhong, M. Zielinski, A. Žídek, V. Bapst, P. Kohli, M. Jaderberg, D. Hassabis, J. M. Jumper, Accurate structure prediction of biomolecular interactions with AlphaFold 3. *Nature* **630**, 493–500 (2024). doi:10.1038/s41586-024-07487-w Medline
63. S. Passaro, G. Corso, J. Wohlwend, M. Reveiz, S. Thaler, V. R. Somnath, N. Getz, T. Portnoi, J. Roy, H. Stark, D. Kwabi-Addo, D. Beaini, T. Jaakkola, R. Barzilay, Boltz-2: Towards accurate and efficient binding affinity prediction. bioRxiv 659707 [Preprint] (2025); https://doi.org/10.1101/2025.06.14.659707.
64. S. Kubo, C. S. Black, E. Joachimiak, S. K. Yang, T. Legal, K. Peri, A. A. Z. Khalifa, A. Ghanaeian, C. L. McCafferty, M. Valente-Paterno, C. De Bellis, P. M. Huynh, Z. Fan, E. M. Marcotte, D. Wloga, K. H. Bui, Native doublet microtubules from *Tetrahymena thermophila* reveal the importance of outer junction proteins. *Nat. Commun.* **14**, 2168 (2023). doi:10.1038/s41467-023-37868-0 Medline
65. A. Waterhouse, M. Bertoni, S. Bienert, G. Studer, G. Tauriello, R. Gumienny, F. T. Heer, T. A. P. de Beer, C. Rempfer, L. Bordoli, R. Lepore, T. Schwede, SWISS-MODEL: Homology modelling of protein structures and complexes. *Nucleic Acids Res.* **46**, W296–W303 (2018). doi:10.1093/nar/gky427 Medline
66. A. Brown, F. Long, R. A. Nicholls, J. Toots, P. Emsley, G. Murshudov, Tools for macromolecular model building and refinement into electron cryo-microscopy reconstructions. *Acta Crystallogr. D Biol. Crystallogr.* **71**, 136–153 (2015). doi:10.1107/S1399004714021683 Medline
67. P. V. Afonine, B. K. Poon, R. J. Read, O. V. Sobolev, T. C. Terwilliger, A. Urzhumtsev, P. D. Adams, Real-space refinement in PHENIX for cryo-EM and crystallography. *Acta Crystallogr. D Struct. Biol.* **74**, 531–544 (2018). doi:10.1107/S2059798318006551 Medline
68. C. J. Williams, J. J. Headd, N. W. Moriarty, M. G. Prisant, L. L. Videau, L. N. Deis, V. Verma, D. A. Keedy, B. J. Hintze, V. B. Chen, S. Jain, S. M. Lewis, W. B. Arendall 3rd, J. Snoeyink, P. D. Adams, S. C. Lovell, J. S. Richardson, D. C. Richardson, MolProbity: More and better reference data for improved all-atom structure validation. *Protein Sci.* **27**, 293–315 (2018). doi:10.1002/pro.3330 Medline
69. D. Gambarotto, F. U. Zwettler, M. Le Guennec, M. Schmidt-Cernohorska, D. Fortun, S. Borgers, J. Heine, J.-G. Schloetel, M. Reuss, M. Unser, E. S. Boyden, M. Sauer, V. Hamel, P. Guichard, Imaging cellular ultrastructures using expansion microscopy (U-ExM). *Nat. Methods* **16**, 71–74 (2019). doi:10.1038/s41592-018-0238-1 Medline
70. J. Schindelin, I. Arganda-Carreras, E. Frise, V. Kaynig, M. Longair, T. Pietzsch, S. Preibisch, C. Rueden, S. Saalfeld, B. Schmid, J.-Y. Tinevez, D. J. White, V. Hartenstein, K. Eliceiri, P. Tomancak, A. Cardona, Fiji: An open-source platform for biological-image analysis. *Nat. Methods* **9**, 676–682 (2012). doi:10.1038/nmeth.2019 Medline
71. M. H. Laporte, D. Gambarotto, É. Bertiaux, L. Bournonville, V. Louvel, J. M. Nunes, S. Borgers, V. Hamel, P. Guichard, Time-series reconstruction of the molecular architecture of human centriole assembly. *Cell* **187**, 2158–2174.e19 (2024). doi:10.1016/j.cell.2024.03.025 Medline
72. S. Richards, N. Aziz, S. Bale, D. Bick, S. Das, J. Gastier-Foster, W. W. Grody, M. Hegde, E. Lyon, E. Spector, K. Voelkerding, H. L. Rehm; ACMG Laboratory Quality Assurance Committee, Standards and guidelines for the interpretation of sequence variants: A joint consensus recommendation of the American College of Medical Genetics and Genomics and the Association for Molecular Pathology. *Genet. Med.* **17**, 405–424 (2015). doi:10.1038/gim.2015.30 Medline
73. J. Wallmeier, D. Bracht, H. S. Alsaif, G. W. Dougherty, H. Olbrich, S. Cindric, M. Dzietko, C. Heyer, N. Teig, C. Thiels, E. Faqeih, A. Al-Hashim, S. Khan, I. Mogarri, M. Almannai, W. Al Otaibi, F. S. Alkuraya, C. Koerner-Rettberg, H. Omran, Mutations in TP73 cause impaired mucociliary clearance and lissencephaly. *Am. J. Hum. Genet.* **108**, 1318–1329 (2021). doi:10.1016/j.ajhg.2021.05.002 Medline

Downloaded from https://www.science.org at Cornell University on September 14, 2026

74. American Thoracic Society; European Respiratory Society, ATS/ERS recommendations for standardized procedures for the online and offline measurement of exhaled lower respiratory nitric oxide and nasal nitric oxide, 2005. *Am. J. Respir. Crit. Care Med.* **171**, 912–930 (2005). doi:10.1164/rccm.200406-710ST Medline
75. C. Allan, J.-M. Burel, J. Moore, C. Blackburn, M. Linkert, S. Loynton, D. Macdonald, W. J. Moore, C. Neves, A. Patterson, M. Porter, A. Tarkowska, B. Loranger, J. Avondo, I. Lagerstedt, L. Lianas, S. Leo, K. Hands, R. T. Hay, A. Patwardhan, C. Best, G. J. Kleywegt, G. Zanetti, J. R. Swedlow, OMERO: Flexible, model-driven data management for experimental biology. *Nat. Methods* **9**, 245–253 (2012). doi:10.1038/nmeth.1896 Medline
76. M. Fliegauf, J. Horvath, C. von Schnakenburg, H. Olbrich, D. Müller, J. Thumfart, B. Schermer, G. J. Pazour, H. P. H. Neumann, H. Zentgraf, T. Benzing, H. Omran, Nephrocystin specifically localizes to the transition zone of renal and respiratory cilia and photoreceptor connecting cilia. *J. Am. Soc. Nephrol.* **17**, 2424–2433 (2006). doi:10.1681/ASN.2005121351 Medline
77. W. F. Chissoe, E. L. Vezey, J. J. Skvarla, The use of osmium-thiocarbohydrazide for structural stabilization and enhancement of secondary electron images in scanning electron microscopy of pollen. *Grana* **34**, 317–324 (1995). doi:10.1080/00173139509429065
78. A. Shoemark, M. Boon, C. Brochhausen, Z. Bukowy-Bieryllo, M. M. De Santi, P. Goggin, P. Griffin, R. G. Hegele, R. A. Hirst, M. W. Leigh, A. Lupton, K. MacKenney, H. Omran, J.-C. Pache, A. Pinto, F. P. Reinholt, J. Schroeder, P. Yiallouros, E. Escudier; representing the BEAT-PCD Network Guideline Development Group, International consensus guideline for reporting transmission electron microscopy results in the diagnosis of primary ciliary dyskinesia (BEAT PCD TEM Criteria). *Eur. Respir. J.* **55**, 1900725 (2020). doi:10.1183/13993003.00725-2019 Medline
79. J. H. Sisson, J. A. Stoner, B. A. Ammons, T. A. Wyatt, All-digital image capture and whole-field analysis of ciliary beat frequency. *J. Microsc.* **211**, 103–111 (2003). doi:10.1046/j.1365-2818.2003.01209.x Medline
80. I. Letunic, P. Bork, Interactive Tree of Life (iTOL) v6: Recent updates to the phylogenetic tree display and annotation tool. *Nucleic Acids Res.* **52**, W78–W82 (2024). doi:10.1093/nar/gkae268 Medline
81. B. Yariv, E. Yariv, A. Kessel, G. Masrati, A. B. Chorin, E. Martz, I. Mayrose, T. Pupko, N. Ben-Tal, Using evolutionary data to make sense of macromolecules with a "face-lifted" ConSurf. *Protein Sci.* **32**, e4582 (2023). doi:10.1002/pro.4582 Medline
82. F. Sievers, A. Wilm, D. Dineen, T. J. Gibson, K. Karplus, W. Li, R. Lopez, H. McWilliam, M. Remmert, J. Söding, J. D. Thompson, D. G. Higgins, Fast, scalable generation of high-quality protein multiple sequence alignments using Clustal Omega. *Mol. Syst. Biol.* **7**, 539 (2011). doi:10.1038/msb.2011.75 Medline
83. N. D. Ulrich, Y. C. Shen, Q. Ma, K. Yang, D. F. Hannum, A. Jones, J. Machlin, J. F. Randolph Jr., Y. R. Smith, S. B. Schon, A. Shikanov, E. E. Marsh, R. Lieberman, S. J. Gurczynski, B. B. Moore, J. Z. Li, S. Hammoud, Cellular heterogeneity of human fallopian tubes in normal and hydrosalpinx disease states identified using scRNA-seq. *Dev. Cell* **57**, 914–929.e7 (2022). doi:10.1016/j.devcel.2022.02.017 Medline
84. Q. Liang, X. Cheng, J. Wang, L. Owen, A. Shakoor, J. L. Lillvis, C. Zhang, M. Farkas, I. K. Kim, Y. Li, M. DeAngelis, R. Chen, A multi-omics atlas of the human retina at single-cell resolution. *Cell Genom.* **3**, 100298 (2023). doi:10.1016/j.xgen.2023.100298 Medline
85. Y. Kuwata, K. Yasuda, K. Tsukita, A. Kikuya, N. Takayama, N. Yanagida, K. Kimura, R. Takahashi, R. Matsumoto, T. Maki, Characterizing hypoxia-orchestrated post-stroke changes in oligodendrocyte precursor cells for optimized cell therapy. *Stem Cell Reports* **20**, 102687 (2025). doi:10.1016/j.stemcr.2025.102687 Medline
86. M. Steinegger, J. Söding, MMseqs2 enables sensitive protein sequence searching for the analysis of massive data sets. *Nat. Biotechnol.* **35**, 1026–1028 (2017). doi:10.1038/nbt.3988 Medline
87. J. Jumper, R. Evans, A. Pritzel, T. Green, M. Figurnov, O. Ronneberger, K. Tunyasuvunakool, R. Bates, A. Žídek, A. Potapenko, A. Bridgland, C. Meyer, S. A. A. Kohl, A. J. Ballard, A. Cowie, B. Romera-Paredes, S. Nikolov, R. Jain, J. Adler, T. Back, S. Petersen, D. Reiman, E. Clancy, M. Zielinski, M. Steinegger, M. Pacholska, T. Berghammer, S. Bodenstein, D. Silver, O. Vinyals, A. W. Senior, K. Kavukcuoglu, P. Kohli, D. Hassabis, Highly accurate protein structure prediction with AlphaFold. *Nature* **596**, 583–589 (2021). doi:10.1038/s41586-021-03819-2 Medline
88. M. Mirdita, K. Schütze, Y. Moriwaki, L. Heo, S. Ovchinnikov, M. Steinegger, ColabFold: Making protein folding accessible to all. *Nat. Methods* **19**, 679–682 (2022). doi:10.1038/s41592-022-01488-1 Medline
89. E. W. Schmid, J. C. Walter, Predictomes, a classifier-curated database of AlphaFold-modeled protein-protein interactions. *Mol. Cell* **85**, 1216–1232.e5 (2025). doi:10.1016/j.molcel.2025.01.034 Medline
90. V. Satopää, J. Albrecht, D. Irwin, B. Raghavan, "Finding a 'kneedle' in a haystack: detecting knee points in system behavior" in *2011 31st International Conference on Distributed Computing Systems Workshops, Minneapolis, MN, USA, 2011* (IEEE, 2011), pp. 166–171; https://doi.org/10.1109/ICDCSW.2011.20.
91. K. Labun, T. G. Montague, M. Krause, Y. N. Torres Cleuren, H. Tjeldnes, E. Valen, CHOPCHOP v3: Expanding the CRISPR web toolbox beyond genome editing. *Nucleic Acids Res.* **47**, W171–W174 (2019). doi:10.1093/nar/gkz365 Medline
92. K. J. Livak, T. D. Schmittgen, Analysis of relative gene expression data using real-time quantitative PCR and the 2(-Δ Δ C(T)) method. *Methods* **25**, 402–408 (2001). doi:10.1006/meth.2001.1262 Medline
93. J. Wallmeier, D. Frank, A. Shoemark, T. Nöthe-Menchen, S. Cindric, H. Olbrich, N. T. Loges, I. Aprea, G. W. Dougherty, P. Pennekamp, T. Kaiser, H. M. Mitchison, C. Hogg, S. B. Carr, M. A. Zariwala, T. Ferkol, M. W. Leigh, S. D. Davis, J. Atkinson, S. K. Dutcher, M. R. Knowles, H. Thiele, J. Altmüller, H. Krenz, M. Wöste, A. Brentrup, F. Ahrens, C. Vogelberg, D. J. Morris-Rosendahl, H. Omran, De novo mutations in FOXJ1 result in a motile ciliopathy with hydrocephalus and randomization of left/right body asymmetry. *Am. J. Hum. Genet.* **105**, 1030–1039 (2019). doi:10.1016/j.ajhg.2019.09.022 Medline
94. H. Zhou, L. Terbeck, A. Berical, M. Brunet, S. M. Lange, J. R. Anderson, H. Olbrich, D. C. Bracht, K. Wohlgemuth, C. Rieck, J. Raidt, J. Klingauf, S. Sutharsan, H. Mussaffi, D. Prais, V. Dunphy, S. T. Homma, P. Guichard, V. Hamel, F. J. Hawkins, H. Omran, A. Brown, Source code for: In situ structure of the human ciliary transition zone links linker defects to primary ciliary dyskinesia, Zenodo (2026); https://doi.org/10.5281/zenodo.18845738.

ACKNOWLEDGMENTS

We are deeply grateful to the individuals with PCD and their families for participating in this study. Cryo-ET data were collected at the Harvard Cryo-EM Center for Structural Biology at Harvard Medical School. We thank Conny Leistner for assistance with FIB-SEM and tomogram segmentation; Alister Burt for technical support with Warp 2; Maria Ericsson and the staff of the Harvard Medical School Electron Microscopy Facility for their assistance with TEM and SEM imaging; and SBGrid for computing support. We are also grateful for the support of Ulrike Keller from the Institute of Medical Physics and Biophysics (IMPB) at Münster University Hospital. We thank Thomas Zobel, Sarah Weischer and Jens Wendt of the MÜNSTER IMAGING NETWORK of the University of Münster for microscopy support. We also thank Andreas Borgscheiper, Borami Shin, Dörthe Thüß, Mareike Dahmer-Heath, Sebastian George, Hanna Hakenes, Simone Helms, Petra Pennekamp, Maria Tekaat, Maren Später (Sanobis GmbH) and Dominik Otto (Sanobis GmbH) for technical assistance. **Funding:** Cystic Fibrosis Foundation grants BERICA22Q0 and BERICA22G0 (A.Be); Emily's Entourage (A.Be); Swiss State Secretariat for Education, Research and Innovation (SERI) contract MB22.00075 (M.B., P.G.); National Institutes of Health grant P01 HL170952 (F.J.H.); Deutsche Forschungsgemeinschaft (DFG) grants OM6/7, OM6/8, OM6/10, CRU 326 OM6/11, OM6/14, OM6/23, and Collaborative Research Centre 'Reproduction.MS' (SFB 1748, project number 549467913) (H.O., J.R.); Bundesministerium für Forschung, Technologie und Raumfahrt (BMFTR) grant 01GM2203A, NEOCYST (H.O., P.P.); Bundesministerium für Forschung, Technologie und Raumfahrt (BMFTR) grant 01GR2303, ReproTrackMS (H.O., J.R.); Deutsche Forschungsgemeinschaft (DFG) grant OL450/1 (H.Ol.); Deutsche Forschungsgemeinschaft (DFG) grant OL459/3 (H.Ol.); National Institutes of Health grant R35 GM161402 (A.B.); Smith Family Foundation (A.B.); Giovanni Armenise Harvard Foundation (A.B.). **Author contributions:** H.Z. performed all structural biology steps, including ALI culture preparation, data acquisition, tomogram reconstruction, subtomogram averaging, protein identification, and atomic model building. J.R.A. performed subtomogram averaging of distal TZ DMTs. H.Z. performed biochemical validation. L.T., C.R., K.W., and D.C.B. performed cellular analyses. L.T., S.M.L., and J.K. were responsible for TEM and SEM analyses. Genetic analyses were

Downloaded from https://www.science.org at Cornell University on September 14, 2026

performed by H.OI. and L.T. Statistical analysis of ALI cultures was performed by K.W. A.Be, H.Z., and V.D. generated *ECT2L*-KO cultures, supervised by F.J.H. M.B. performed U-ExM, supervised by P.G. and V.H. S.T.H. conducted immunoblot analysis of *ECT2L*-KO cultures. J.R., S.S., H.M., D.P., and H.O. performed and interpreted clinical investigations. A.B. supervised the structural work, and H.O. oversaw all human-related studies. H.Z., L.T., H.O. and A.B. wrote the paper. All authors critically reviewed and edited the final version. **Competing interests:** Authors declare that they have no competing interests. **Data, code, and materials availability**: The cell lines generated and presented in this manuscript (*ECT2L*-KO and wild-type iPSC-derived basal cells) are available from the authors upon reasonable request. Composite, consensus and focused refinement density maps for the human transition zone doublet microtubule (TZ DMT) are available in the Electron Microscopy Data Bank (EMDB; https://www.ebi.ac.uk/pdbe/emdb/) under accession codes EMD-76188 (composite), EMD-75919 (consensus), EMD-75912, EMD-75913, EMD-75916, EMD-75917, and EMD-75920. Maps for the TZ linker are available under EMD-76173 (composite), EMD-76171 (consensus), EMD-75914, EMD-75915, EMD-75918, and EMD-75921. Corresponding atomic models are in the Protein Data Bank (PDB; https://www.rcsb.org/) under accession codes 11YJ and 11XU. A representative tomogram of the human airway ciliary base (Fig. 1) is deposited in the EMDB under accession code EMD-76272. Source data are provided as Source Data files. Uncropped immunoblots are provided as data S9. The software developed for this study, Tomo_remove_duplicates_napari, is an open-source napari plugin for the visualization and spatial filtering of cryo-ET datasets. The source code is archived on Zenodo (DOI: 10.5281/zenodo.18845738) (*94*). This software is distributed under the BSD 3-Clause License and incorporates foundational components originally developed by Alister Burt (2022, https://github.com/alisterburt/napari-cryo-et-demo). Documentation and installation instructions are provided in the repository. **License information:** Copyright © 2026 the authors, some rights reserved; exclusive licensee American Association for the Advancement of Science. No claim to original US government works. https://www.science.org/about/science-licenses-journal-article-reuse

SUPPLEMENTARY MATERIALS

science.org/doi/10.1126/science.aei5957
Figs. S1 to S21
Tables S1 and S2
MDAR Reproducibility Checklist
Data S1 to S9
Movie S1 and S2

Submitted 5 May 2026; accepted 26 August 2026
Published online 10 September 2026
10.1126/science.aei5957

Downloaded from https://www.science.org at Cornell University on September 14, 2026

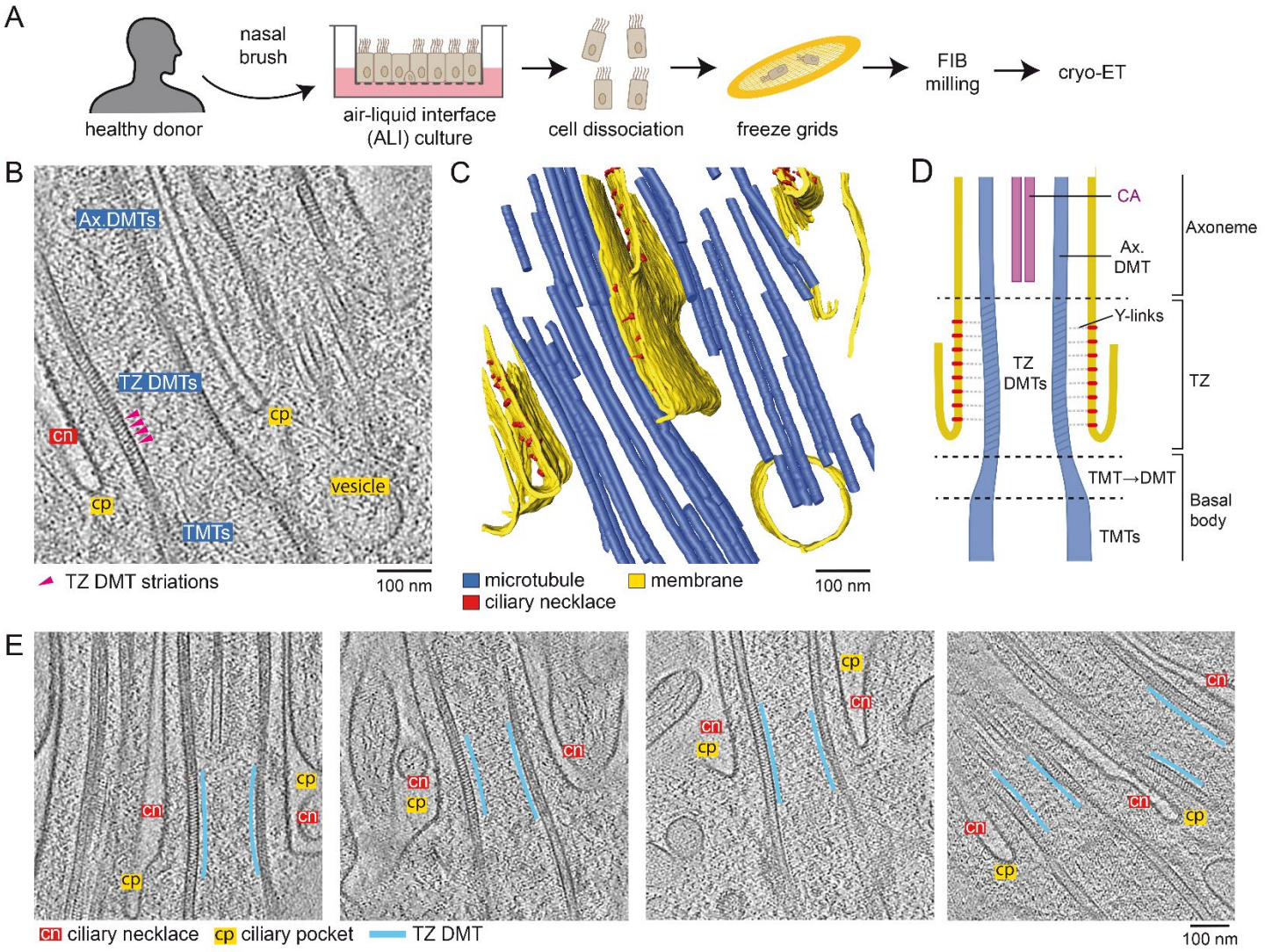

Fig. 1. Cryo-electron tomography of the transition zone in human respiratory cilia. (**A**) Experimental workflow. Basal epithelial cells from nasal brushings were expanded and then differentiated at the air-liquid interface (ALI), then dissociated, applied to EM grids, plunge-frozen, and thinned by focused ion beam (FIB) milling to generate lamellae suitable for cryo-ET. (**B**) Tomographic slice (30 Å thick; 6x binned; Fourier filtered) showing the bases of two neighboring cilia. Pink arrows indicate striations within TZ doublet microtubules (TZ DMTs). Abbreviations: cn, ciliary necklace; cp, ciliary pocket; Ax. DMT, axonemal doublet microtubule; TMT, basal body triplet microtubule. (**C**) Segmentation of the tomogram in (B). Microtubules are shown in blue, membranes in yellow, and ciliary necklace densities in red. (**D**) Longitudinal schematic of the ciliary base delineating the major regions: the axoneme proper with the central apparatus (CA) and axonemal DMTs; the TZ region containing TZ DMTs, the ciliary necklace, and Y links; and the basal body containing TMTs. Dashed horizontal lines indicate boundaries between regions. (**E**) Additional tomographic slices illustrating ciliary pocket diversity. Scale bar, 100 nm.

Downloaded from https://www.science.org at Cornell University on September 14, 2026

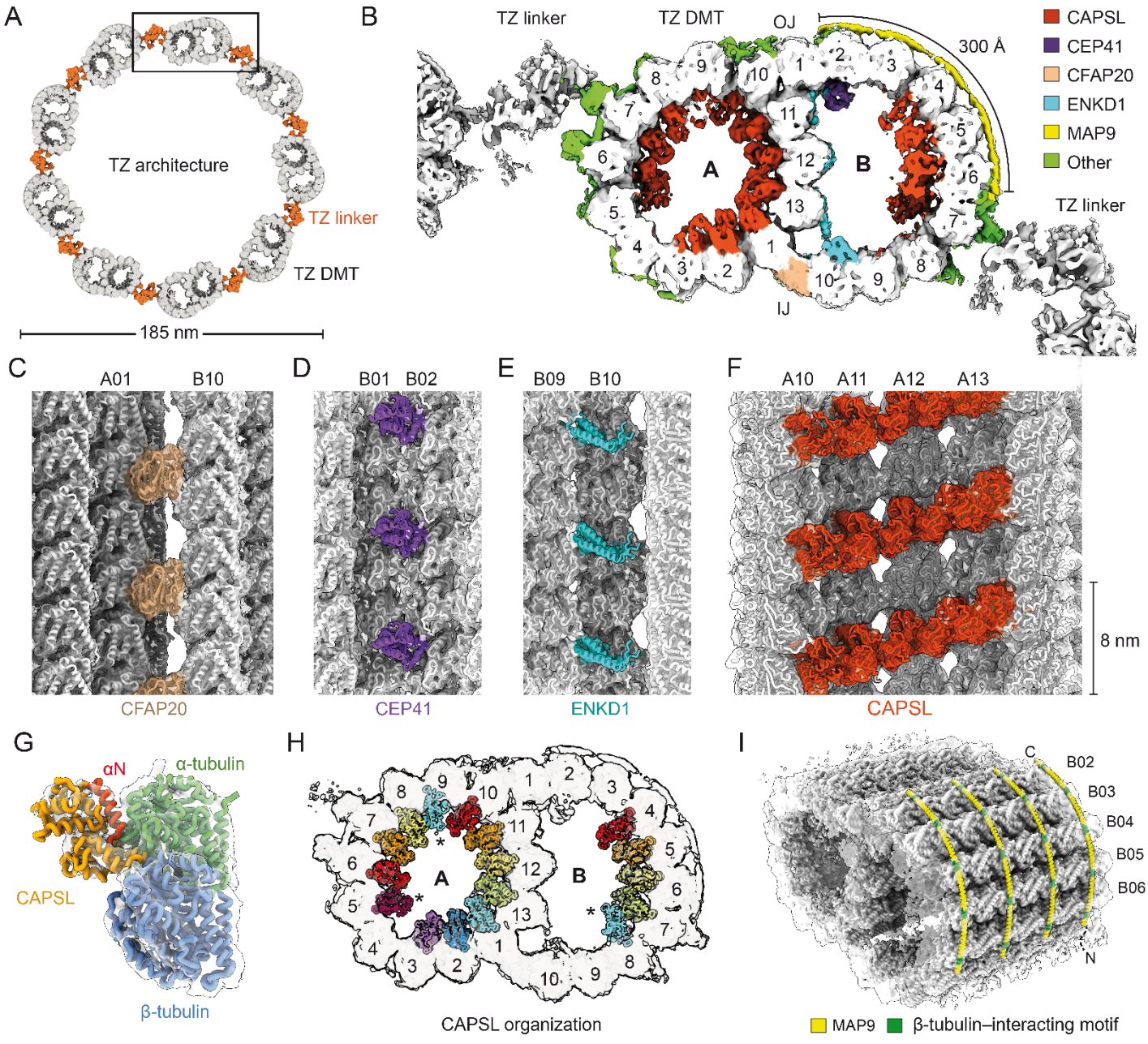

Downloaded from https://www.science.org at Cornell University on September 14, 2026

Fig. 2. Microtubule inner protein (MIP) composition of human TZ doublet microtubules. (**A**) Cross section of an in silico reconstruction of the complete ring of nine TZ DMTs, generated by combining subtomogram averages of a single TZ DMT. Placement was guided by densities corresponding to neighboring DMTs in the TZ linker reconstruction. Box denotes the subtomogram average shown in (B). (**B**) Isosurface representation of the TZ DMT subtomogram average, colored by protein. Abbreviations: OJ, outer junction; IJ, inner junction. (**C**) Density and atomic model of CFAP20 bound at the IJ between protofilaments A01–B10. (**D**) Density and atomic model of CEP41 bound to protofilaments B01–B02 near the OJ. (**E**) Density and atomic model of ENKD1 bound at the interface between protofilaments B09–B10. (**F**) Density and atomic model showing multiple copies of CAPSL bound to protofilaments A10–A13, viewed from the A-tubule lumen. (**G**) Density corresponding to an N-terminal α-helix (αN), present in CAPSL but absent in CAPS and CAPS2, supporting assignment of the shelf-like MIP to CAPSL. (**H**) Organization of CAPSL within the TZ DMT. Transparent isosurface with fitted CAPSL models; colors distinguish individual CAPSL copies, and asterisks mark CAPSL proteins with weak density consistent with substoichiometric binding. (**I**) B-tubule exterior showing four copies of MAP9 (yellow) spaced every 8 nm. The β-tubulin–interacting motif (green) aligns with the presumed β-tubulin-binding sites on B-tubule protofilaments.

Downloaded from https://www.science.org at Cornell University on September 14, 2026

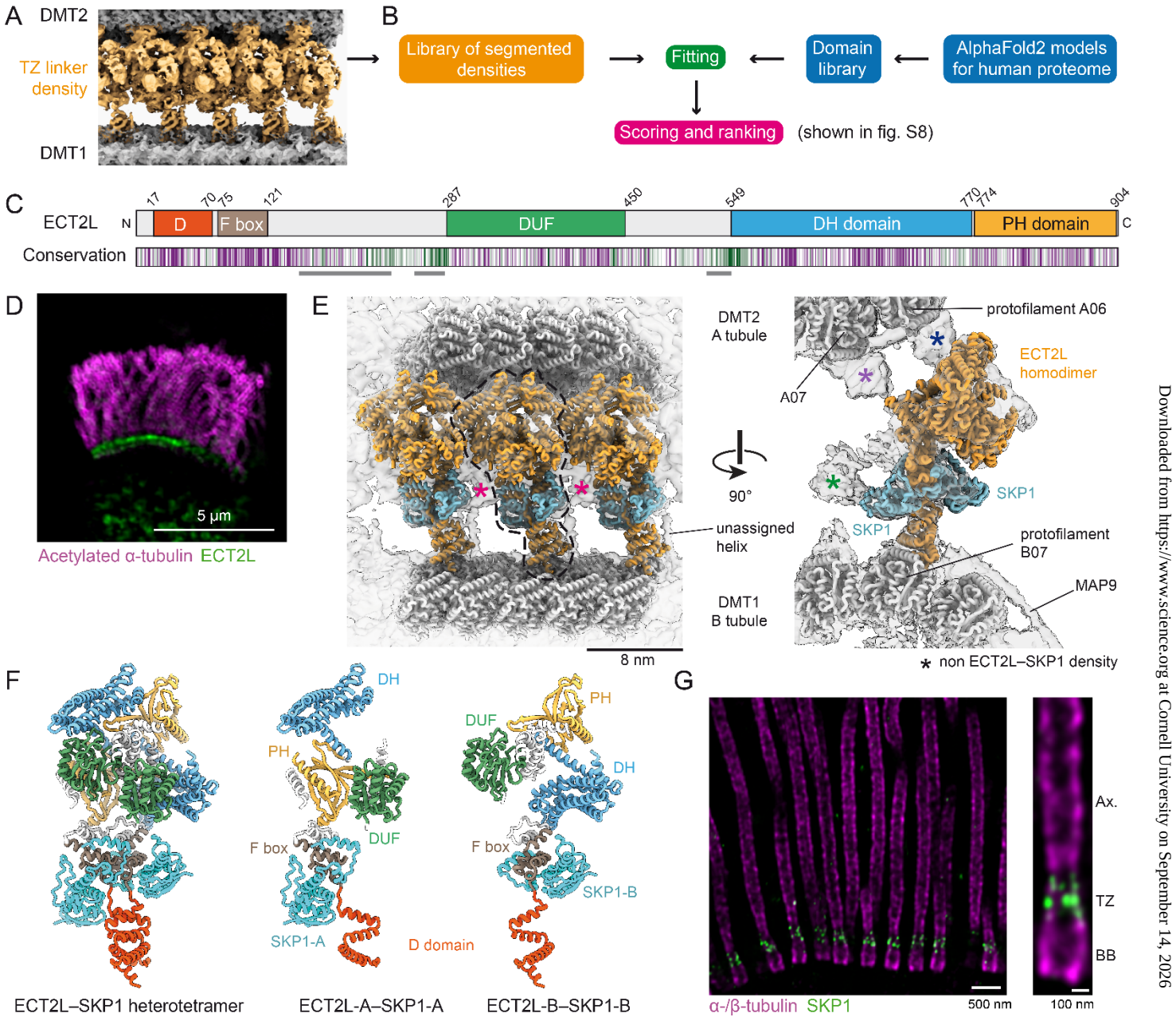

Fig. 3. SKP1-bound ECT2L is a major component of the TZ linker. (**A**) Subtomogram average of a TZ linker array (orange) bridging neighboring doublet microtubules (DMT1 and DMT2, gray). (**B**) Workflow for de novo assignment of TZ linker proteins using domain recognition against a library of AlphaFold2-predicted human protein domains. (**C**) Domain organization of human ECT2L with sequence conservation scores (1–9) plotted below (green, variable; purple, conserved). Unresolved residues (gray underline) are not included in the atomic model. (**D**) Super-resolution immunofluorescence of a healthy respiratory epithelial cell stained with antibodies against acetylated α-tubulin (magenta) and ECT2L (green). Scale bar, 5 µm. (**E**) Orthogonal views of the atomic model of three ECT2L–SKP1 heterotetramers fitted into the TZ linker map. Asterisks mark unassigned density. (**F**) Three-dimensional architecture of the 2:2 ECT2L–SKP1 complex. Left: heterotetramer colored by domain as in (C). Middle and right: individual ECT2L–SKP1 heterodimers showing asymmetric domain arrangements. (**G**) U-ExM of human respiratory motile cilia showing SKP1 localization (green) at the TZ, between the basal body (BB) and axoneme (Ax.). Quantification is provided in fig. S7A. Scale bars, 500 nm (left), 100 nm (right).

Downloaded from https://www.science.org at Cornell University on September 14, 2026

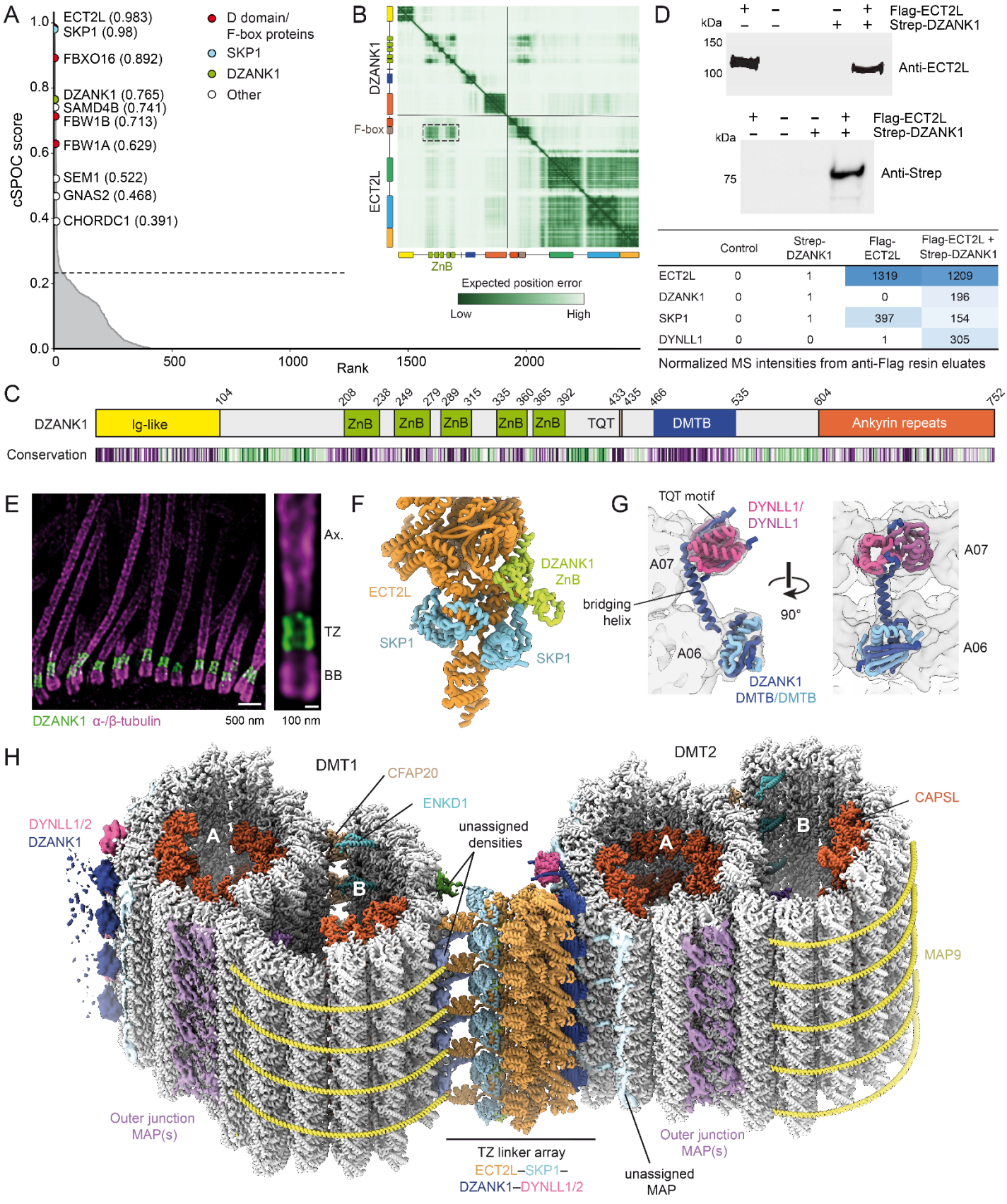

Downloaded from https://www.science.org at Cornell University on September 14, 2026

Fig. 4. Structural basis for the interaction between DZANK1 and ECT2L. (**A**) Rank-ordered cSPOC scores from AlphaFold2-Multimer predictions between ECT2L and 2,363 human ciliary proteins. The dotted line marks the high-confidence threshold; the ten top-scoring hits (colored circles) are labeled. Source data are provided in data S3. (**B**) AlphaFold3 Predicted Aligned Error (PAE) plot for the DZANK1–ECT2L complex. Darker green indicates higher confidence; box highlights the predicted interface between DZANK1 ZnB domains and the ECT2L F-box. (**C**) Domain architecture of human DZANK1 with sequence conservation scores (1–9) plotted below (green, variable; purple, conserved). The protein contains an N-terminal Ig-like domain (yellow), five zinc-binding (ZnB) domains (green), a dimerization and microtubule-binding (DMTB) domain (blue), a TQT motif, and C-terminal ankyrin repeats (orange). (**D**) Co-precipitation of ECT2L with DZANK1. Flag-tagged ECT2L and Strep-tagged DZANK1 were expressed in Expi293F cells and purified on anti-Flag resin. Immunoblots (top, middle) and mass spectrometry (bottom) show that Strep-DZANK1 is recovered only in the presence of Flag-ECT2L and co-expression pulls down endogenous SKP1 and DYNLL1. Source data are provided in data S6. (**E**) U-ExM of human respiratory cilia stained for α-/β-tubulin (magenta) and DZANK1 (green). DZANK1 localization, just distal to the basal body (BB), is consistent with TZ enrichment. Quantification is provided in fig. S7A. Scale bars, 500 nm (left), 100 nm (right). (**F**) Model of DZANK1 ZnB domains bound to the ECT2L–SKP1 complex, matching density that bridges adjacent ECT2L–SKP1 heterotetramers. (**G**) Orthogonal views of the DZANK1 DMTB–DYNLL1 complex fitted to density at the A-tubule interface. (**H**) Atomic model of two TZ DMTs connected by a TZ-linker array. Models are shown as cartoons; unassigned density as isosurface.

Downloaded from https://www.science.org at Cornell University on September 14, 2026

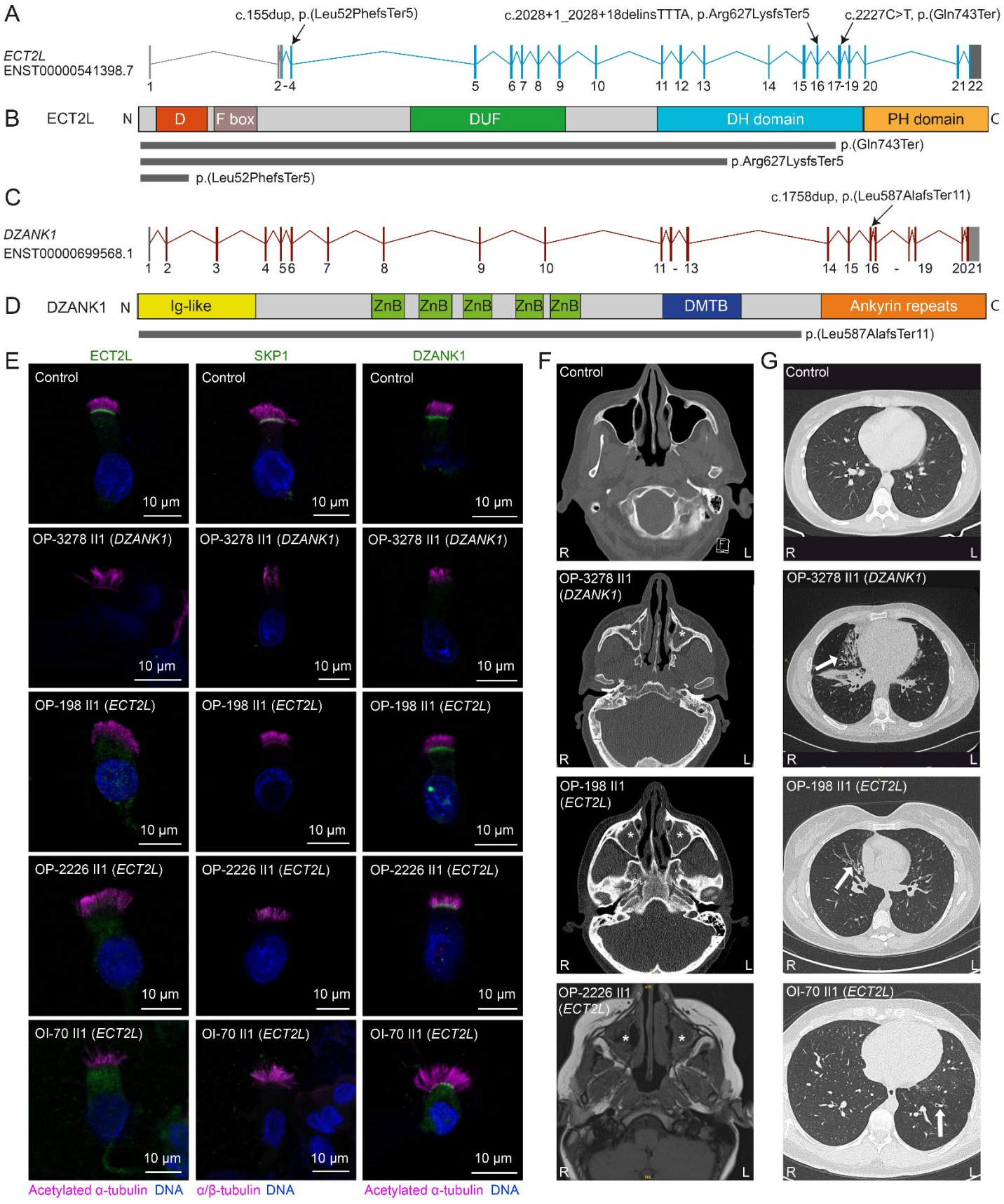

Downloaded from https://www.science.org at Cornell University on September 14, 2026

Fig. 5. *ECT2L* and *DZANK1* variants cause primary ciliary dyskinesia (PCD). (**A**) Genomic structure of *ECT2L* (reference transcript ENST000005541398.7) showing exon-intron organization and positions of PCD-associated variants. (**B**) ECT2L domain architecture with predicted protein consequences of each variant (gray bars). (**C**) Genomic structure of *DZANK1* (reference transcript ENST00000699568.1) and location of the identified PCD-associated variant. (**D**) DZANK1 domain architecture with the predicted protein consequence (gray bar). (**E**) Immunofluorescence of multiciliated respiratory epithelial cells from a healthy control, *DZANK1*-variant individual OP-3278 II1, and *ECT2L*-variant individuals OP-198 II1, OP-2226 II1, and OI-70 II1. Cells were stained for acetylated α-tubulin or α/β-tubulin (magenta) and, from left-to-right, ECT2L, SKP1, or DZANK1 (green). Nuclei are stained with Hoechst 33342 (blue). Individual channels are shown in figs. S15 to S17. Scale bars, 10 μm. (**F**) Axial images through the maxillary sinuses from a healthy control (top), the *DZANK1*-variant individual OP-3278 II1, and *ECT2L*-variant individuals OP-198 II1 and OP-2226 II1 (bottom; CT for control, OP-3278 II1, OP-198 II1; MRI for OP-2226 II1). Patient images show sinus opacification or loss of aeration with mucosal swelling (white asterisks). (**G**) Axial chest CTs from a healthy control (top), the *DZANK1*-variant individual OP-3278 II1, and *ECT2L*-variant individuals OP-198 II1 and OI-70 II1 (bottom), demonstrating bronchial wall thickening and bronchiectasis in the variant individuals (white arrows).

Downloaded from https://www.science.org at Cornell University on September 14, 2026

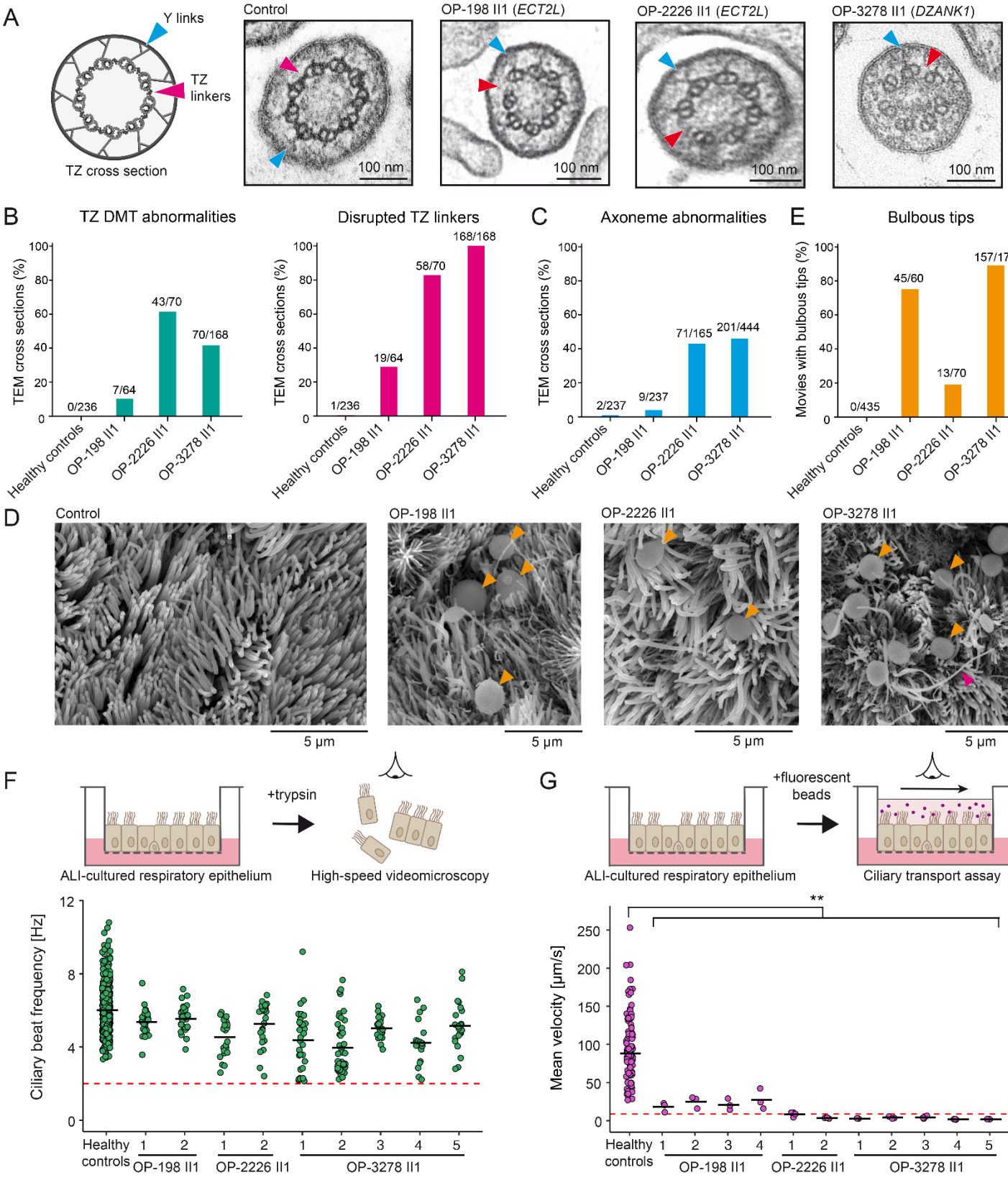

Downloaded from https://www.science.org at Cornell University on September 14, 2026

Fig. 6. *ECT2L* and *DZANK1* variants disrupt TZ architecture and motile cilia function. (**A**) Schematic of the TZ in human motile cilia with representative TEM cross-sections from healthy control epithelium and ALI cultures from *ECT2L*- and *DZANK1*-variant individuals. Y links (blue arrows), TZ linkers (pink arrows), and defects (red arrows) are indicated. (**B**) Quantification of TZ cross-sections showing abnormal TZ DMT organization (left) or disrupted TZ linkers (right). Numbers above bars indicate sections with the defect/total sections. (**C**) Quantification of axonemal cross-sections with disorganized 9+2 structure. (**D**) SEM of ALI cultures from a healthy control, *ECT2L*-variant individuals OP-198 II1 and OP-2226 II1, and *DZANK1*-variant individual OP-3278 II1. Orange arrows mark bulbous ciliary tips; pink arrow marks an elongated cilium. Scale bars, 5 µm. (**E**) Percentage of high-speed videos of trypsinized ALI cultures showing cilia with bulbous tips. Numbers above bars indicate movies with bulbous tips/total movies. (**F**) Ciliary beat frequencies (CBFs) from high-speed videomicroscopy of trypsinized ALI cultures. Data represent two or more biological replicates (independent ALI cultures). Variant CBFs fall within the normal range. The 2-Hz detection threshold of the assay is indicated (red dashed line). Each data point represents one movie. Source data are provided in data S7. (**G**) Ciliary transport of fluorescent particles in ALI cultures. Top: schematic. Bottom: mean velocities of fluorescent particles across the epithelial surface from two or more biological replicates (independent ALI cultures). Transport is reduced in cultures from OP-198 II1 (26.0% of control), OP-2226 II1 (6.8%), and OP-3278 II1 (3.4%) (Mann-Whitney U test, $^{**}P = 0.0013$). The background flow induced by the microscope lamp is indicated (red dashed line). Each data point represents one transwell. Source data are provided in data S8.

Downloaded from https://www.science.org at Cornell University on September 14, 2026

Science
AAAS

In situ structure of the human ciliary transition zone links linker defects to primary ciliary dyskinesia

Haixia Zhou, Lea Terbeck, Andrew Berical, Marine Brunet, Sven M. Lange, Jacob R. Anderson, Heike Olbrich, Diana Carolin Bracht, Kai Wohlgemuth, Cynthia Rieck, Johanna Raidt, Jürgen Klingauf, Sivagurunathan Sutharsan, Huda Mussaffi, Dario Prais, Victoria Dunphy, Sachiko T. Homma, Paul Guichard, Virginie Hamel, Finn J. Hawkins, Heymut Omran, and Alan Brown

*Science***Ahead of Print** DOI: 10.1126/science.aei5957

View the article online
https://www.science.org/doi/10.1126/science.aei5957
Permissions
https://www.science.org/help/reprints-and-permissions

Downloaded from https://www.science.org at Cornell University on September 14, 2026

Use of this article is subject to the Terms of service

Science (ISSN 1095-9203) is published by the American Association for the Advancement of Science. 1200 New York Avenue NW, Washington, DC 20005. The title *Science* is a registered trademark of AAAS.

Copyright © 2026 The Authors, some rights reserved; exclusive licensee American Association for the Advancement of Science. No claim to original U.S. Government Works